Fundamental Actuation Properties of Multirotors: Force–Moment Decoupling and Fail–Safe Robustness

Giulia Michieletto, Markus Ryll, *Member, IEEE*, and Antonio Franchi, *Senior Member, IEEE*

***Abstract*—In this paper, we shed light on two fundamental actuation capabilities of multirotors. The first is the degree of coupling between the total force and total moment generated by the propellers. The second is the ability to robustly fly completely still in place after the loss of one or more propellers, in the case of monodirectional propellers. These are formalized through the definition of some algebraic conditions on the control allocation matrices. The theory is valid for any multirotor, with arbitrary number, position, and orientation of the propellers. As a show case for the general theory, we demonstrate that standard star-shaped hexarotors with collinear propellers are not able to robustly fly completely still at a constant spot using only five of their six propellers. To deeply understand this counterintuitive result, it is enough to apply our theory, which clarifies the role of the tilt angles and locations of the propellers. The theory is also able to explain why, on the contrary, both the tilted star-shaped and the Y-shaped hexarotors can fly with only five out of six propellers. The analysis is validated with both simulations and extensive experimental results showing recovery control after rotor losses.**

***Index Terms*—Aerospace control, aircraft propulsion, aerial robotics, motion control, unmanned aerial vehicles.**

I. Introduction

QUADROTORS constitute the most common unmanned aerial vehicle (UAV) currently used in the civil and industrial context. Their high versatility allows their application field to range from exploration and mapping to grasping, from monitoring and surveillance to transportation [1]–[4]. Physical interaction for quadrotors has been enabled by theoretical tools such as physical property reshaping [5] and external wrench estimation [6]. Nevertheless, the interest of robotic communities is now moving toward modeling, design, and control of more complex multirotor platforms, where the number of propellers is larger than four [7]–[12]. Several hexarotor and octorotor vehicles have been recently presented for applications spanning from multiagent cooperative manipulation (see, e.g., [13] and the references within) to human and environment interaction (see, e.g., [14]–[16]). Intuitively, the intrinsic redundancy of these platforms can be exploited in order to enhance fundamental actuation properties as the possibility to independently control the position and the attitude of the vehicle and the robustness to rotor-failures, which constitute key requirements for the real-world deployment. However, having a redundant number of propellers is not in general enough to allow a static and safe hovering (i.e., a hovering in which both the linear and the angular velocity are zero) as it can be seen, for example, in [17], where experiments are shown in which the hexarotor starts to spin when control of a propeller is lost, even if still five propellers are available[1] and from other commercially available platforms.[2] A more in-depth theoretical understanding of the fundamental actuation properties of multirotors is needed to handle those critical and extremely important situations.

The six rotor case has received particular attention. In order to ensure full actuation, recent works have presented new designs based on a tilt-rotor architecture, whose effectiveness has been exhaustively validated even considering quadrotor platforms (see, e.g., [18] and [19]). In [20], it has been shown that a standard star-shaped hexarotor can gain the 6-DoF actuation using only one additional servomotor that allows to equally tilt all propellers in a synchronized way.

It has been proven that in the case of rotor-loss the propellers' mutual orientations affect the hexarotor control properties. For example, Du *et al.* [21] have conducted a *controllability* analysis based on the multirotor linear approximation around hovering. They concluded that in the case of a rotor failure the controllability strongly depends on the propeller spinning directions. Similarly, in [22], the concept of *maneuverability* has been introduced and investigated for a star-shaped hexarotor having tilted rotors. Maneuverability has been defined in terms of maximum acceleration achievable in the 6 DoFs. In the failed-motor case, the (vertical) maneuverability reduces due to the loss in control authority, and the hovering condition is still possible only for some tilt of the propellers. In [23], the authors have instead proposed a method to design a star-shaped hexarotor keeping the ability to reject disturbance torques in all directions while

Manuscript received September 7, 2017; revised November 21, 2017; accepted February 12, 2018. Date of publication May 15, 2018; date of current version June 6, 2018. This paper was recommended for publication by Associate Editor S. Shen and Editor T. Murphey upon evaluation of the reviewers' comments. This work was partially supported by the European Union's Horizon 2020 research and innovation program under Grant 644271 AEROARMS. The work of G. Michieletto was supported by the Eiffel Excellence Scholarship Programme of the French Ministry of Foreign Affairs and International Development. The work of M. Ryll was supported by the German Research Foundation (DFG). *(Corresponding author: Antonio Franchi.)*

G. Michieletto is with the LAAS-CNRS, Université de Toulouse, CNRS, Toulouse 31400, France, and also with the Department of Information Engineering, University of Padova, Padova 35131, Italy (e-mail: giulia.michieletto@unipd.it).

M. Ryll and A. Franchi are with the LAAS-CNRS, Université de Toulouse, CNRS, Toulouse 31400, France (e-mail: Ryll.Markus@gmail.com; antonio.franchi@laas.fr).

This paper has supplementary downloadable material available at http://ieeexplore.ieee.org.

Color versions of one or more of the figures in this paper are available online at http://ieeexplore.ieee.org.

Digital Object Identifier 10.1109/TRO.2018.2821155

[1] See the video here: https://youtu.be/cocvUrPfyfo.

[2] See, e.g., the video here: https://youtu.be/HQ7wa5cBT_w?t=45.

counteracting the effect of a failure in any motor. Their solution rests on (inward/outward) tilting all the propellers of a small fixed angle. Finally, in [24], we investigated the robustness of star-shaped hexarotors as their capability to still achieve the static hovering condition (constant position and orientation) after a rotor loss, concluding that tilted platforms are 1-loss robust and providing also a suitable cascaded control law for failed vehicles. In that paper only numerical simulation results have been provided. In this paper, we aim at significantly pushing forward the theoretical understanding on the actuation properties of multirotor UAVs and at experimentally corroborating the developed theory.

Introducing an appropriate dynamic model, we first investigate the coupling between the control force and the control moment that emerges from the intrinsic cascaded dependence of the UAVs translational dynamics from the rotation one. We derive some necessary conditions on the control input space that imply the possibility to independently act on the vehicle position and attitude. To validate our statements, we analyze the fulfillment of this property for platforms known in the literature and categorize them using a proposed taxonomy.

As second step, we formalize the concept of rotor-failure robustness for multirotors with propellers that can produce lift force in only one direction (by far the most common situation). This is based on the possibility for a multirotor to hover in a constant spot with zero linear and angular velocity (*static hovering realizability* property) even in the case a propeller fails and stops spinning, while being able to produce a full set of control inputs in any direction. The developed theory can be applied to any multirotor structure comprising any number of propellers arranged in any possible way.

In particular, we applied the theory to hexarotor platforms, since they are the most interesting ones. This led to an extensive discussion on the robustness/vulnerability properties of these platforms. The generic hexarotor structure considered is parametrized by three angles that determine the positions (w.r.t. the platform center of mass (CoM)) and the spinning axes direction of the six propellers in order to span the most known classes of hexarotors. The study of the role of these angles shows that both the tilted star-shaped hexarotor and Y-shaped hexarotor can still hover statically after a rotor-loss. These conclusions are supported by simulative and experimental results.

The remainder of the paper is organized as follows. The dynamic model for the generically tilted multirotors is given in Section II. Section III is devoted to the analysis of the force–moment decoupling properties. An in-depth rotor-failure robustness analysis for hexarotor platforms is conducted in Section V, after the formalization of the concept of static hovering realizability in Section IV. Then, Section VI and Section VII, respectively, report the experimental and simulative results of the control of failed six-rotors. Main conclusions and future research directions are drawn in Section VIII.

II. Generically Tilted Multirotors

A Generically Tilted Multirotor (GTM) is an aerial vehicle consisting of a rigid body and n lightweight propellers. The model of a GTM is derived in the following for the reader's convenience and to fix the nomenclature.

Considering the body frame $\mathscr{F}_B = \{O_B, (\mathbf{x}_B, \mathbf{y}_B, \mathbf{z}_B)\}$ attached to the platform such that the origin O_B coincides with its CoM, the full-pose of the vehicle in world frame $\mathscr{F}_W$ is described by the pair $\mathbf{q} = (\mathbf{p}, \mathbf{R}) \in SE(3)$, where $\mathbf{p} \in \mathbb{R}^3$ is the position of O_B in $\mathscr{F}_W$, and the rotation matrix $\mathbf{R} \in SO(3)$ represents the orientation of $\mathscr{F}_B$ w.r.t. $\mathscr{F}_W$. The linear velocity of O_B in $\mathscr{F}_W$ is $\mathbf{v} = \dot{\mathbf{p}} \in \mathbb{R}^3$, whereas the orientation kinematics is governed by the nonlinear relation

$$\dot{\mathbf{R}} = \mathbf{R}[\boldsymbol{\omega}]_\times \tag{1}$$

where $\boldsymbol{\omega} \in \mathbb{R}^3$ is the angular velocity of $\mathscr{F}_B$ w.r.t. $\mathscr{F}_W$, expressed in $\mathscr{F}_B$, and $[\cdot]_\times$ is the map associating any vector in $\mathbb{R}^3$ to the corresponding skew-symmetric matrix in $\mathfrak{so}(3)$.

The ith propeller, with $i = 1 \dots n$, rotates with an angular velocity $\boldsymbol{\omega}_i \in \mathbb{R}^3$ about a spinning axis that passes through the propeller center O_{P_i}. Both the direction of $\boldsymbol{\omega}_i$ and the position $\mathbf{p}_i \in \mathbb{R}^3$ of O_{P_i} are assumed constant in $\mathscr{F}_B$, while any assumption is allowed on the angular velocity sign accounting, e.g., for both bidirectional (unconstrained) and mono-directional (constrained) propellers.[3] As customary, the propeller applies at O_{P_i} a thrust (or lift) force $\mathbf{f}_i \in \mathbb{R}^3$ that is equal to

$$\mathbf{f}_i = \kappa c_{f_i} \|\boldsymbol{\omega}_i\| \boldsymbol{\omega}_i \tag{2}$$

where $c_{f_i} > 0$ is the norm of $\mathbf{f}_i$ when $\|\boldsymbol{\omega}_i\| = 1$ and $\kappa \in \{-1, 1\}$. Both c_{f_i} and κ are constant parameters depending on the shape of the propeller. The propeller is said of CCW type if $\kappa = 1$ and of CW type if $\kappa = -1$. For CCW propellers, the lift has the same direction of the angular velocity of the propeller, while for the CW, it has the opposite direction. Moreover the ith propeller generates a drag moment $\boldsymbol{\tau}_i^d \in \mathbb{R}^3$ whose direction is always opposite to the angular velocity of the propeller

$$\boldsymbol{\tau}_i^d = -c_{\tau_i}^+ \|\boldsymbol{\omega}_i\| \boldsymbol{\omega}_i \tag{3}$$

where $c_{\tau_i}^+ > 0$ is the norm of $\boldsymbol{\tau}_i^d$ when $\|\boldsymbol{\omega}_i\| = 1$. Also $c_{\tau_i}^+$ is a constant parameter depending on the shape of the propeller. We assume that the propeller is lightweight enough that the associated inertia moment can be neglected w.r.t. the two main aerodynamical effects just described and the platform inertia.

One can arbitrarily choose a unit direction vector $\mathbf{z}_{P_i} \in \mathbb{R}^3$ that is parallel to the ith propeller spinning axis and constant in $\mathscr{F}_B$. The angular velocity is then expressed as $\boldsymbol{\omega}_i = (\boldsymbol{\omega}_i^\top \mathbf{z}_{P_i}) \mathbf{z}_{P_i} =: \omega_i \mathbf{z}_{P_i}$. The quantity $\omega_i \in \mathbb{R}$ is the propeller *spinning rate*. Substituting this last expression in (2) and (3) we obtain

$$\mathbf{f}_i = \kappa c_{f_i} |\omega_i| \omega_i \mathbf{z}_{P_i} = c_{f_i} u_i \mathbf{z}_{P_i} \tag{4}$$

$$\boldsymbol{\tau}_i^d = -c_{\tau_i}^+ |\omega_i| \omega_i \mathbf{z}_{P_i} = c_{\tau_i} u_i \mathbf{z}_{P_i} \tag{5}$$

where $u_i = \kappa |\omega_i| \omega_i$ and $c_{\tau_i} = -\kappa c_{\tau_i}^+$. The input $u_i \in \mathbb{R}$, a one-to-one mapping with ω_i, appears linearly in the force and moment equation. The type of propeller is understood by the sign of c_{τ_i} ($c_{\tau_i} < 0$ for CCW and $c_{\tau_i} > 0$ for CW).

[3] In Section. IV, we shall restrict this model to the case of mono-directional propellers for studying the fail–safe robustness of most common platforms.

Denoting with $\boldsymbol{\tau}_i^t = \mathbf{p}_i \times \mathbf{f}_i \in \mathbb{R}^3$ the thrust moment of the ith propeller, the total control force $\mathbf{f}_c \in \mathbb{R}^3$ and control moment $\boldsymbol{\tau}_c \in \mathbb{R}^3$ applied at O_B and expressed in $\mathscr{F}_B$ are

$$\mathbf{f}_c = \sum_{i=1}^{n} \mathbf{f}_i = \sum_{i=1}^{n} c_{f_i} \mathbf{z}_{P_i} u_i \tag{6}$$

$$\boldsymbol{\tau}_c = \sum_{i=1}^{n} (\boldsymbol{\tau}_i^t + \boldsymbol{\tau}_i^d) = \sum_{i=1}^{n} (c_{f_i} \mathbf{p}_i \times \mathbf{z}_{P_i} + c_{\tau_i} \mathbf{z}_{P_i}) u_i. \tag{7}$$

Introducing the control input vector $\mathbf{u} = [\, u_1 \ \cdots \ u_n \,]^\top \in \mathbb{R}^n$, (6) and (7) are shortened as

$$\mathbf{f}_c = \mathbf{F}_1 \mathbf{u}, \quad \text{and} \quad \boldsymbol{\tau}_c = \mathbf{F}_2 \mathbf{u} \tag{8}$$

where the *control force input matrix* $\mathbf{F}_1 \in \mathbb{R}^{3\times n}$ and the *control moment input matrix* $\mathbf{F}_2 \in \mathbb{R}^{3\times n}$ depend on the geometric and aerodynamic parameters introduced before.

The facts that $c_{f_i} > 0$ and $c_{\tau_i}^+ > 0$ imply that none of the columns of both $\mathbf{F}_1$ and $\mathbf{F}_2$ is a zero vector, and therefore, we have both $\operatorname{rank}(\mathbf{F}_1) \geq 1$ and $\operatorname{rank}(\mathbf{F}_2) \geq 1$ by construction.

Neglecting the second-order effects (such as, the gyroscopic and inertial effects due to the rotors, the flapping, and the rotor drag), the dynamics of the GTM is described by the following system of Newton–Euler equations:

$$m\ddot{\mathbf{p}} = -mg\mathbf{e}_3 + \mathbf{R}\mathbf{f}_c = -mg\mathbf{e}_3 + \mathbf{R}\mathbf{F}_1\mathbf{u} \tag{9}$$

$$\mathbf{J}\dot{\boldsymbol{\omega}} = -\boldsymbol{\omega} \times \mathbf{J}\boldsymbol{\omega} + \boldsymbol{\tau}_c = -\boldsymbol{\omega} \times \mathbf{J}\boldsymbol{\omega} + \mathbf{F}_2\mathbf{u} \tag{10}$$

where $g > 0$, $m > 0$, and $\mathbf{J} \in \mathbb{R}^{3\times 3}$ are the gravitational acceleration, the total mass of the platform, and its positive definite inertia matrix, respectively, and $\mathbf{e}_i$ is the ith canonical basis vector of $\mathbb{R}^3$ with $i = 1, 2, 3$.

III. Decoupling of Force and Moment

In the following, we assume that the GTM satisfies

$$\operatorname{rank}(\mathbf{F}_2) = 3. \tag{11}$$

The input space $\mathbb{R}^n$ can always be partitioned in the orthogonal subspaces $\operatorname{Im}(\mathbf{F}_2^\top)$ and $\operatorname{Im}(\mathbf{F}_2^\top)^\perp = \ker(\mathbf{F}_2)$, such that the vector $\mathbf{u}$ can be rewritten as the sum of two terms, namely

$$\mathbf{u} = \mathbf{T}_2\tilde{\mathbf{u}} = [\mathbf{A}_2 \ \ \mathbf{B}_2] \begin{bmatrix} \tilde{\mathbf{u}}_A \\ \tilde{\mathbf{u}}_B \end{bmatrix} = \mathbf{A}_2\tilde{\mathbf{u}}_A + \mathbf{B}_2\tilde{\mathbf{u}}_B \tag{12}$$

where $\mathbf{T}_2 = [\mathbf{A}_2 \ \mathbf{B}_2] \in \mathbb{R}^{n\times n}$ is an orthogonal matrix such that $\operatorname{Im}(\mathbf{A}_2) = \operatorname{Im}(\mathbf{F}_2^\top)$ and $\operatorname{Im}(\mathbf{B}_2) = \ker(\mathbf{F}_2)$. Note that, thanks to (11), $\mathbf{A}_2 \in \mathbb{R}^{n\times 3}$ is full rank, i.e., $\operatorname{rank}(\mathbf{A}_2) = 3$, while $\mathbf{B}_2 \in \mathbb{R}^{n\times n-3}$ has $\operatorname{rank}(\mathbf{B}_2) = n - 3$. Given this partition, we have

$$\boldsymbol{\tau}_c = \mathbf{F}_2\mathbf{T}_2\tilde{\mathbf{u}} = \mathbf{F}_2\mathbf{A}_2\tilde{\mathbf{u}}_A \tag{13}$$

$$\mathbf{f}_c = \mathbf{F}_1\mathbf{T}_2\tilde{\mathbf{u}} = \mathbf{F}_1\mathbf{A}_2\tilde{\mathbf{u}}_A + \mathbf{F}_1\mathbf{B}_2\tilde{\mathbf{u}}_B =: \mathbf{f}_c^A + \mathbf{f}_c^B. \tag{14}$$

The matrix $\mathbf{F}_2\mathbf{A}_2$ in (13) is nonsingular thus any moment $\boldsymbol{\tau} \in \mathbb{R}^3$ can be virtually implemented by setting $\tilde{\mathbf{u}}_A = (\mathbf{F}_2\mathbf{A}_2)^{-1}\boldsymbol{\tau}$ in (12) in conjunction with any $\tilde{\mathbf{u}}_B \in \mathbb{R}^{n-3}$.

The control force, which obviously belongs to $\mathfrak{F} := \operatorname{Im}(\mathbf{F}_1)$, is split in two components: $\mathbf{f}_c = \mathbf{f}_c^A + \mathbf{f}_c^B$, defined in (14). The component $\mathbf{f}_c^A = \mathbf{F}_1\mathbf{A}_2\tilde{\mathbf{u}}_A$ represents the "spurious" force generated by the allocation of the input needed to obtain a nonzero control moment. This component belongs to the subspace $\mathfrak{F}_A := \operatorname{Im}(\mathbf{F}_1\mathbf{A}_2) \subseteq \mathbb{R}^3$. The component $\mathbf{f}_c^B = \mathbf{F}_1\mathbf{B}_2\tilde{\mathbf{u}}_B$ instead represents a force that can be assigned independently from the control moment by allocating the input $\mathbf{u}$ in $\operatorname{Im}(\mathbf{B}_2) = \ker(\mathbf{F}_2)$. This "free" force component belongs to the subspace $\mathfrak{F}_B := \operatorname{Im}(\mathbf{F}_1\mathbf{B}_2) \subseteq \mathbb{R}^3$, and it is obtained by assigning $\tilde{\mathbf{u}}_B$. Being $\mathbf{T}_2$ nonsingular, we have that $\mathfrak{F} = \mathfrak{F}_A + \mathfrak{F}_B$. It is instrumental to recall that $1 \leq \dim\mathfrak{F} \leq 3$ because $\operatorname{rank}(\mathbf{F}_1) \geq 1$, and that $\mathfrak{F}_B \subseteq \mathfrak{F}$, thus $\dim\mathfrak{F} \geq \dim\mathfrak{F}_B$.

The dimension of $\mathfrak{F}_B$ and its relation with $\mathfrak{F}$ sheds light upon the GTM actuation capabilities. The following two sets of definitions are devoted to this purpose.

Definition 1: A GTM is

1) *fully coupled* (FC) if $\dim\mathfrak{F}_B = 0$ (i.e., if $\mathbf{F}_1\mathbf{B}_2 = \mathbf{0}$),
2) *partially coupled* (PC) if $\dim\mathfrak{F}_B \in \{1, 2\}$ and $\mathfrak{F}_B \subsetneq \mathfrak{F}$,
3) *un-coupled* (UC), or fully decoupled, if $\mathfrak{F}_B = \mathfrak{F}$ (or, equivalently, $\mathfrak{F}_A \subseteq \mathfrak{F}_B$).

In an FC GTM, the control force depends completely upon the implemented control moment, in fact $\mathbf{f}_c^B = \mathbf{0}$, and thus, $\mathbf{f}_c = \mathbf{f}_c^A$. In a PC GTM the projection of the control force onto $\mathfrak{F}_B$ can be chosen freely while the projection onto $\mathfrak{F}_B^\perp \cap \mathfrak{F}$ depends completely upon the implemented control moment. Finally in a UC GTM no projection of the control force depends on the control moment, i.e., the control force can be freely assigned in the whole space $\mathfrak{F}$. Notice that the full decoupling does not imply necessarily that the control force can be chosen in the whole $\mathbb{R}^3$, unless it holds also $\mathfrak{F} = \mathbb{R}^3$.

The second important classification is provided in the following definition.

Definition 2: A GTM

1) has a *decoupled direction* (D1) if $\dim\mathfrak{F}_B \geq 1$
2) has a *decoupled plane* (D2) if $\dim\mathfrak{F}_B \geq 2$
3) is *fully actuated* (D3) if $\dim\mathfrak{F}_B = 3$.

Combining the previous definitions we say that a GTM

1) has a *single decoupled direction* (SD1) if $\dim\mathfrak{F}_B = 1$
2) has a *single decoupled plane* (SD2) if $\dim\mathfrak{F}_B = 2$.

If a GTM has a decoupled direction, then there exists at least a direction along which the projection of the control force can be chosen freely from the control moment. If a GTM has a decoupled plane, then there exists at least a plane over which the projection of the control force can be chosen freely from the control moment. If a GTM is fully actuated, then the control force can be chosen in all $\mathbb{R}^3$ freely from the control moment.

We shall show that the D3 definition is equivalent to the more common definition known in the literature, i.e.,

$$\operatorname{rank}(\mathbf{F}) = \operatorname{rank}\left(\begin{bmatrix} \mathbf{F}_1 \\ \mathbf{F}_2 \end{bmatrix}\right) = 6. \tag{15}$$

Postmultiplying $\mathbf{F}$ by $\mathbf{T}$ does not change the rank, we obtain

$$\mathbf{F}\mathbf{T} = \begin{bmatrix} \mathbf{F}_1 \\ \mathbf{F}_2 \end{bmatrix} [\mathbf{A}_2 \ \mathbf{B}_2] = \begin{bmatrix} \mathbf{F}_1\mathbf{A}_2 & \mathbf{F}_1\mathbf{B}_2 \\ \mathbf{F}_2\mathbf{A}_2 & \mathbf{0} \end{bmatrix}. \tag{16}$$

Recalling that $\operatorname{rank}(\mathbf{F}_2\mathbf{A}_2) = 3$, thanks to (11), we have that $\operatorname{rank}(\mathbf{F}) = 6$ if and only if $\operatorname{rank}(\mathbf{F}_1\mathbf{B}_2) = 3$, which corresponds to the fully actuated definition given above.

In terms of relations between the above-mentioned definitions, we note that: D3 implies UC, while the converse is not

TABLE I
FUNDAMENTAL PROPERTIES OF THE ACTUATION OF A GTM, WHERE N/A DENOTES AN IMPOSSIBLE COMBINATION

		∃ decoupled direction		
			∃ decoupled plane	
	$\dim\mathfrak{F}_B = 0$	$\dim\mathfrak{F}_B = 1$	$\dim\mathfrak{F}_B = 2$	$\dim\mathfrak{F}_B = 3$
$\mathfrak{F}_B \subsetneq \mathfrak{F}$	FC	PC and SD1	PC and SD2	N/A
$\mathfrak{F}_B = \mathfrak{F}$	N/A	UC and SD1	UC and SD2	D3 (UC)
	$(\dim\mathfrak{F} \geq 1)$	$(\dim\mathfrak{F} \geq 1)$	$(\Rightarrow \dim\mathfrak{F} \geq 2)$	$(\Rightarrow \dim\mathfrak{F} = 3)$

true; D3 implies D2; D2 implies D1. Finally, D1 (and thus D2) can coexist with PC or UC but not with FC. Note that in the state-of-the-art of multirotor controllers, it is implicitly assumed that the GTM is fully decoupled and there exists a decoupled direction oriented along its $\mathbf{z}_B$ axis. An exception is represented by controller that we proposed in [24], where the decoupled direction can be any and the GTM can be also PC.

Table I yields a comprehensive view of all aforementioned definitions and relations. In the following, we provide two illustrative examples of GMT and study their coupling properties with the theoretical tools just introduced.

A. Standard (Collinear) Multirotors

Consider that $\mathrm{Im}(\mathbf{F}_1^\top) \subseteq \ker(\mathbf{F}_2) = \mathrm{Im}(\mathbf{B}_2)$. Recalling that $\mathbf{F}_1 \neq \mathbf{0}$, we have that $\mathbf{F}_1\mathbf{B}_2 \neq \mathbf{0}$ and that

$$\mathbf{F}_2\mathbf{F}_1^\top = \mathbf{0} \Leftrightarrow \mathbf{F}_1\mathbf{F}_2^\top = \mathbf{0} \Leftrightarrow \mathbf{F}_1\mathbf{A}_2 = \mathbf{0} \tag{17}$$

therefore, $\mathfrak{F}_A = \{\mathbf{0}\}$, and hence, $\mathfrak{F}_B = \mathfrak{F}$, i.e., the GMT is UC.

Classical multirotor systems fall in this case. They are characterized by an even number of propellers having parallel orientations, a balanced geometry and choice of CW/CCW types. Specifically, as $\mathbf{z}_{P_i} = \mathbf{z}_P$, their matrices $\mathbf{F}_1$ and $\mathbf{F}_2$ result to be

$$\mathbf{F}_1 = \begin{bmatrix} c_{f_1}\mathbf{z}_P \cdots c_{f_n}\mathbf{z}_P \end{bmatrix}$$

$$\mathbf{F}_2 = \begin{bmatrix} c_{f_1}\mathbf{p}_1 \times \mathbf{z}_P \cdots c_{f_n}\mathbf{p}_n \times \mathbf{z}_P \end{bmatrix} + \begin{bmatrix} c_{\tau_1}\mathbf{z}_P \cdots c_{\tau_n}\mathbf{z}_P \end{bmatrix}. \tag{18}$$

Notice, to have $\mathrm{rank}(\mathbf{F}_2) = 3$, it is enough to choose at least the position vectors of two propellers i and j such that $\mathbf{p}_i \times \mathbf{z}_P$, $\mathbf{p}_j \times \mathbf{z}_P$, and $\mathbf{z}_P$ are linearly independent.

To show that $\mathbf{F}_2\mathbf{F}_1^\top = \mathbf{0}$, it has to be observed first that $\mathbf{F}_2\mathbf{F}_1^\top = \mathbf{C}_f + \mathbf{C}_\tau$, where $\mathbf{C}_f = ((\sum_{i=1}^n c_{f_i}^2\mathbf{p}_i) \times \mathbf{z}_P)\mathbf{z}_P^\top \in \mathbb{R}^{3\times3}$ and $\mathbf{C}_\tau = (\sum_{i=1}^n c_{\tau_i}c_{f_i})\mathbf{z}_P\mathbf{z}_P^\top \in \mathbb{R}^{3\times3}$. Then, by suitably choosing the positions and the coefficients $\{c_{\tau_i}, c_{f_i}\}$ one can easily make $\mathbf{C}_f = \mathbf{C}_\tau = \mathbf{0}$. For example, it is enough to make the propellers pairwise balanced, i.e., satisfying $\mathbf{p}_i + \mathbf{p}_j = \mathbf{0}$, $c_{f_i} = c_{f_j}$, and $c_{\tau_i} = -c_{\tau_j}$ for $i \in \{1 \dots \frac{n}{2}\}$ and $j = i + \frac{n}{2}$. Many other choices are however possible.

Finally, w.r.t. Table I, we can note that such a multirotor system has also a decoupled direction but not a decoupled plane, because $\mathrm{rank}(\mathbf{F}_1) = 1$, and thus, $\dim\mathfrak{F}_B = 1$. Classical multirotor systems are therefore un-coupled/fully decoupled (UC) GTMs with a single decoupled direction (SD1).

In these platforms, control moment and control force can be considered independently. Furthermore, two other properties have been fundamental to establish the success and simplicity in controlling such platforms. First of all, the control force is always directed in the same direction in the body frame, regardless of the value of the input $\mathbf{u}$, and therefore, its direction is not affected by the unavoidable uncertainty of the propeller spinning rate. Second of all, the force direction in the world frame can be reliably measured by simple attitude estimation, as well as its derivative (by a gyroscope) and controlled through the fully actuated rotational dynamics. The only price to pay is underactuation ($\dim\mathfrak{F} = 1$), which has not been an obstacle in many cases of practical relevance.

B. Tilted Quadrotor

The tilted quadrotor used in [25] constitutes an example of a kind of vehicle is such that the ith propeller is tilted about the axis joining O_B with O_{P_i} of an angle α_i in a way that the consecutive rotors are oriented in a opposite way, i.e., $\alpha_1 = \alpha_3 = \alpha$ and $\alpha_2 = \alpha_4 = -\alpha$, with $\alpha \in [0, \frac{\pi}{2}]$. Hence, assuming that all the propellers have the same aerodynamic features (namely $c_{f_i} = c_f$ and $|c_{\tau_i}| = c_\tau$), we have

$$\mathbf{F}_1 = c_f \begin{bmatrix} 0 & s\alpha & 0 & -s\alpha \\ s\alpha & 0 & -s\alpha & 0 \\ c\alpha & c\alpha & c\alpha & c\alpha \end{bmatrix} \tag{19}$$

$$\mathbf{F}_2 = c_\tau \begin{bmatrix} 0 & s\alpha + rc\alpha & 0 & -s\alpha - rc\alpha \\ -s\alpha - rc\alpha & 0 & s\alpha + rc\alpha & 0 \\ -c\alpha + rs\alpha & c\alpha - rs\alpha & -c\alpha + rs\alpha & c\alpha - rs\alpha \end{bmatrix} \tag{20}$$

where $r = (c_f/c_\tau)l$ with l denoting the distance between O_B and O_{P_i}, $s\alpha = \sin\alpha$, and $c\alpha = \cos\alpha$.

From (20), it is easy to see that $\mathfrak{F} = \mathbb{R}^3$ if $s\alpha \neq 0$ and $c\alpha \neq 0$, while $\mathfrak{F} = \mathrm{span}\{\mathbf{e}_3\}$ if $s\alpha = 0$, and finally $\mathfrak{F} = \mathrm{span}\{\mathbf{e}_1, \mathbf{e}_2\}$ if $c\alpha = 0$. In addition, $\mathbf{F}_2$ in (20) results to be full rank if $\tan\alpha \neq -r$ and $\tan\alpha \neq \frac{1}{r}$, whereas if $\tan\alpha = \frac{1}{r}$ $(-c\alpha + rs\alpha = 0)$, then $\mathrm{rank}(\mathbf{F}_2) = 2$ and if $\tan\alpha = -r$ $(s\alpha + rc\alpha = 0)$, then $\mathrm{rank}(\mathbf{F}_2) = 1$. When $\mathrm{rank}(\mathbf{F}_2) = 3$, according to (12), the input space $\mathbb{R}^4$ can be partitioned by choosing, for example,

$$\mathbf{A}_2 = \begin{bmatrix} 0 & -1 & -1 \\ 1 & 0 & 1 \\ 0 & 1 & -1 \\ -1 & 0 & 1 \end{bmatrix} \quad \text{and} \quad \mathbf{B}_2 = \begin{bmatrix} 1 \\ 1 \\ 1 \\ 1 \end{bmatrix}. \tag{21}$$

As a consequence, we get

$$\mathbf{F}_1\mathbf{A}_2 = 2c_f \begin{bmatrix} s\alpha & 0 & 0 \\ 0 & -s\alpha & 0 \\ 0 & 0 & 0 \end{bmatrix} \text{ and } \quad \mathbf{F}_1\mathbf{B}_2 = 4c_f \begin{bmatrix} 0 \\ 0 \\ c\alpha \end{bmatrix}. \quad (22)$$

When $c\alpha = 0$, the GTM is FC because $\dim \mathfrak{F}_B = 0$. Instead, as long as $c\alpha \neq 0$, we have that $\dim \mathfrak{F}_B = \mathrm{Im}(\mathbf{F}_1\mathbf{B}_2) = 1$, i.e., the GTM has a SD1, which is $\mathbf{e}_3$. In this case, the platform is UC if and only if $s\alpha = 0$, in fact only in this case $\mathfrak{F}_B = \mathfrak{F}$ (or equivalently $\mathfrak{F}_A = \{\mathbf{0}\} \subseteq \mathfrak{F}_B$). Instead, in the case in which $s\alpha \neq 0$ (as in [25]) the GMT is PC. The plane $\mathfrak{F}_B^{\perp} \cap \mathfrak{F} = \mathrm{span}\{\mathbf{e}_1, \mathbf{e}_2\}$ represents the plane along which the projection of the control force depends completely on the choice of the control moment. In [25], the effect of this term is partially mitigated by the robustness of the hovering controller, however the perfect tracking that is possible with $\alpha = 0$ is theoretically not guaranteed anymore.

IV. Static Hovering Realizability With Mono-Directional Propeller Spin

The large majority of propellers used in GTMs can spin only in one direction, mainly due to the larger efficiency of propellers with asymmetric profile and the difficulty in reliably and quickly changing the spinning direction. It is therefore important to consider this additional constraint in the model and analyze the consequences. In the following, we use the notation $\mathbf{u} \geq \mathbf{0}$ or $\mathbf{u} > \mathbf{0}$ to indicate that each entry of the vector $\mathbf{u}$ is nonnegative or positive, this section, we aim at theoretically analyzing the conditions under which a GTM can stay in a controlled static equilibrium when the additional constraint $\mathbf{u} \geq \mathbf{0}$ is enforced. We start from the following definition.

Definition 3 (Equilibrium): A GTM is in equilibrium if

$$\dot{\mathbf{p}} = \mathbf{0}, \quad \ddot{\mathbf{p}} = \mathbf{0}, \quad \boldsymbol{\omega} = \mathbf{0}, \quad \dot{\boldsymbol{\omega}} = \mathbf{0} \quad (23)$$

or, equivalently

$$\dot{\mathbf{p}} = \mathbf{0},\ \mathbf{f}_c = \mathbf{F}_1\mathbf{u} = mg\mathbf{R}^{\top}\mathbf{e}_3,\ \boldsymbol{\omega} = \mathbf{0},\ \boldsymbol{\tau}_c = \mathbf{F}_2\mathbf{u} = \mathbf{0}. \quad (24)$$

A basic property to ensure the rejection of external disturbances while being in equilibrium is the possibility to exert a control moment $\boldsymbol{\tau}_c$ in any direction and with any intensity by a suitable allocation of the input vector $\mathbf{u} \geq \mathbf{0}$. In this perspective, in [23], the following condition has been introduced.

Definition 4 (Realizability of any control moment [23]): A GTM can realize any control moment if it is possible to allocate the actuator values $\mathbf{u} \geq \mathbf{0}$ to obtain any $\boldsymbol{\tau}_c \in \mathbb{R}^3$. Formally if

$$\forall \boldsymbol{\tau}_c \in \mathbb{R}^3 \quad \exists \mathbf{u} \geq \mathbf{0} \quad \text{s.t.} \quad \mathbf{F}_2\mathbf{u} = \boldsymbol{\tau}_c. \quad (25)$$

In [23], it has been shown that (25) is equivalent to the simultaneous satisfaction of (11) and the following condition:

$$\exists \mathbf{u} > \mathbf{0} \quad \text{s.t.} \quad \mathbf{F}_2\mathbf{u} = \mathbf{0}. \quad (26)$$

A drawback of Definition 4 is to consider only the realizability w.r.t. the control moment, thus ignoring the control force. However, a proper control force generation is also needed to robustly control the GTM while in equilibrium. For this reason, in [24], we have proposed the following additional condition.

Definition 5 (Realizability of any control force [24]): A GTM can realize any control force if it is possible to allocate the input to obtain a control force with any intensity $f_c \in \mathbb{R}_{\geq 0}$ while the platform is in static hovering, i.e., if

$$\forall f_c \in \mathbb{R}_{\geq 0} \quad \exists \mathbf{u} \geq \mathbf{0} \ \text{ s.t. } \mathbf{F}_2\mathbf{u} = \mathbf{0} \ \text{ and } \ \|\mathbf{F}_1\mathbf{u}\| = f_c. \quad (27)$$

Note that the static hovering equilibrium (24) does not force the vehicle in a certain orientation. As a consequence, when it is possible to generate a control force with any nonnegative intensity, then it is sufficient to attain the suitable attitude (orientation) in order to realize any other control force vector.

Proposition 1: Condition (27) is equivalent to

$$\exists \mathbf{u} \geq \mathbf{0} \quad \text{s.t.} \quad \mathbf{F}_2\mathbf{u} = \mathbf{0} \ \text{ and } \ \mathbf{F}_1\mathbf{u} \neq \mathbf{0}. \quad (28)$$

Proof: The proof is rather straightforward.

(28) $\Rightarrow$ (27): Assume that $\bar{\mathbf{u}}$ satisfies (28), i.e., $\mathbf{F}_2\bar{\mathbf{u}} = \mathbf{0}$ and $\mathbf{F}_1\bar{\mathbf{u}} \neq \mathbf{0}$, then, for any $f_c \in \mathbb{R}_{\geq 0}$, it exists the vector $\mathbf{u} = f_c\bar{\mathbf{u}}/\|\mathbf{F}_1\bar{\mathbf{u}}\|$, which satisfies (27).

(27) $\Rightarrow$ (28): Consider any $f_c \geq 0$, and assume that $\mathbf{u}$ satisfies (27), then the same $\mathbf{u}$ satisfies also (28). ■

Exploiting the previous equivalent conditions, we introduce the following more complete definition for the realizability of the static hovering.

Definition 6 (Static hovering realizability): If the three conditions (11), (26), and (28) are met then the GTM can realize a static hover (with nonnegative inputs), or equivalently, is statically hoverable.

Notice that (11), (26), and (28) are only necessary conditions to ensure that a platform can stay in any equilibrium according to Definition 3.

The property of realizability of static hovering is agnostic w.r.t. the set of attitudes at which the static hovering can be realized. These are all the attitudes represented by a matrix $\mathbf{R}$ for which (24) holds with $\mathbf{u} \geq \mathbf{0}$. If a GTM can hover statically, we are sure that at least one attitude of such kind exists.

All the common star-shaped multirotors are GTM that can hover statically, as stated in the following proposition.

Proposition 2: Multirotors having n propellers, with $n \geq 4$ and even, $c_{\tau_i} = c_\tau > 0$ for $i = 1, 3 \ldots n-1$, $c_{\tau_i} = -c_\tau$ for $i = 2, 4 \ldots n$, and $c_{f_i} = c_f > 0$, $\mathbf{z}_{P_i} = \mathbf{e}_3$, $\mathbf{p}_i = l\,\mathbf{R}_z((i-1)\frac{2\pi}{n})\mathbf{e}_1$ for $i = 1 \ldots n$ (where $l = \mathrm{dist}(O_B, O_{P_i}) > 0$ and $\mathbf{R}_z$ is the canonical rotation matrix about the z-axis) can realize static hovering.

Proof: After some simple algebra, it is easy to check that $\mathbf{F}_2$ is full rank. Furthermore, it is also easy to check that the vector of all ones $\mathbf{1} = [1 \ \cdots \ 1]^{\top} \in \mathbb{R}^n$ has the property that $\mathbf{F}_2\mathbf{1} = \mathbf{0}$ and $\mathbf{F}_1\mathbf{1} \neq \mathbf{0}$, thus $\mathbf{u} = \mathbf{1}$ satisfies all the required conditions. ■

Standard star-shaped multirotors described in Proposition 2 are not the only statically hoverable GTMs. In fact, in Section V, we shall show other examples that arise in the important situations of propeller failures. Conversely, it is also easy to find examples of GTMs that cannot hover statically, like the one in the following Proposition, which also explains why quadrotors have an alternated pattern of CW and CCW propellers.

Proposition 3: Consider a 4-rotor that respects all the conditions in Proposition 2 apart from the fact that $c_{\tau_i} = c_\tau > 0$ for

$i = 1, 2$ and $c_{\tau_i} = -c_\tau$ for $i = 3, 4$. This GTM cannot realize static hovering.

Proof: Expanding (7) for this special case, and noting that $\mathbf{p}_3 = -\mathbf{p}_1$ and $\mathbf{p}_4 = -\mathbf{p}_2$, we obtain

$$\begin{aligned}\boldsymbol{\tau}_c &= \sum_{i=1}^{n} \left(c_{f_i}\,\mathbf{p}_i \times \mathbf{z}_{P_i} + c_{\tau_i}\mathbf{z}_{P_i}\right) u_i \qquad (29)\\ &= \left(c_f\,\mathbf{p}_1 \times \mathbf{e}_3 + c_\tau \mathbf{e}_3\right)(u_1 - u_3)\\ &\quad + \left(c_f\,\mathbf{p}_2 \times \mathbf{e}_3 + c_\tau \mathbf{e}_3\right)(u_2 - u_4).\end{aligned}$$

Denoting with $\mathbf{f}_{21} = (c_f\,\mathbf{p}_1 \times \mathbf{e}_3 + c_\tau \mathbf{e}_3)$ and $\mathbf{f}_{22} = (c_f\,\mathbf{p}_2 \times \mathbf{e}_3 + c_\tau \mathbf{e}_3)$, we have that $\mathbf{F}_2 = [\mathbf{f}_{12}\ \ \mathbf{f}_{22} - \mathbf{f}_{12} - \mathbf{f}_{22}]$ whose rank is 2, and therefore, condition (11) is not met. ■

Notice that if there was no constraint $\mathbf{u} \geq \mathbf{0}$ the capability of realizing static hovering would have been equivalent to the existence of a decoupled direction, while since we are considering the additional constraint $\mathbf{u} \geq \mathbf{0}$ one needs stronger properties to be fulfilled. This remark is in line with the fact that GMTs that can hover statically have a decoupled direction (D1) (see Definition 2) as stated in the following proposition, but are not necessarily un-coupled/fully decoupled (UC).

Proposition 4: A GTM that can realize static hovering has a decoupled direction. In particular, consider any $\mathbf{u} = \bar{\mathbf{u}} \in \mathbb{R}^n$ which satisfies (28), then a possible decoupled direction is

$$\mathbf{d}_* = \mathbf{F}_1 \bar{\mathbf{u}} / \|\mathbf{F}_1 \bar{\mathbf{u}}\|. \qquad (30)$$

Proof: $\bar{\mathbf{u}} \in \ker(\mathbf{F}_2)$ hence the rightmost requirement in (28) can be written as $\mathbf{F}_1 \mathbf{B}_2 \tilde{\mathbf{u}}_B \neq \mathbf{0}$, which implies $\dim \mathfrak{F}_B \geq 1$. ■

V. Rotor-Failure Robustness for Hexarotors

In this section, we apply the theory developed so far to investigate the *rotor-failure robustness* of hexarotor GTMs. Robustness is defined as the capability of the platform to realize static hovering even in the case a propeller fails and stops to spin. The attention is focused on platforms having six rotors, because in [26] it has been shown that it is the minimum number of actuators that guarantees the resolution of controller allocation problem with redundancy against a single failure.

Definition 7: In the context of this paper, "the kth rotor is *failed*" means that it stops to spin ($\omega_k = u_k = 0$), thus producing neither thrust nor drag anymore. A rotor that is not failed, i.e., whose spinning rate can be still controlled, is *healthy*.

Definition 8: Given a hexarotor GTM whose propellers set is denoted by $\mathscr{P} = \{1 \dots 6\}$, this is said to be $\{k\}$-*loss robust* with $k \in \mathscr{P}$ if the GTM possessing only the healthy rotors in $\mathscr{P} \backslash \{k\}$ can still realize static hover (according to Definition 6).

Definition 9: A hexarotor GTM is said to be

1) *fully robust* if it is $\{k\}$-loss robust for *any* $k \in \mathscr{P}$;
2) *partially robust* if it is not fully robust but it is $\{k\}$-loss robust for *at least one* $k \in \mathscr{P}$;
3) *fully vulnerable* if it is neither fully nor partially robust.

A. (α, β, γ)–Hexarotor Family

In the following, we describe a fairly general hexarotor GTM model parametrized by 3 angles: α, β, and γ. The angle γ is meant to define the propellers arrangement, while the angles α and β allow to describe the orientation of the rotors spinning direction (see Fig. 1) as formally explained in the following. The so obtained (α, β, γ)–*hexarotor family* spans (and extends) the most commonly used classes of six-rotor GTMs. Our goal is to analyze the relations that exist between these angles and the robustness features of the members of this family. By doing so, we significantly extend the results presented in [23], where only a family parametrized by β is considered (i.e., it is assumed $\alpha = \gamma = 0$) and only the compliance with Definition 4 is analyzed, instead of the more strict Definition 6.

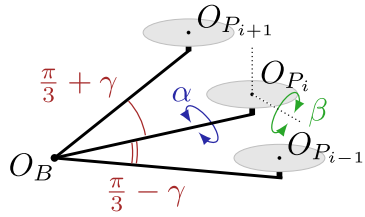

Fig. 1. Arrangement of three consecutive propellers, highlighting the effect of angles α, β, and γ.

For a (α, β, γ)-hexarotor GTM, the positions in $\mathscr{F}_B$ of the propeller centers O_{P_i}s are given by

$$\mathbf{p}_i = \underbrace{\mathbf{R}_z\left((i-1)\tfrac{\pi}{3} - \tfrac{1}{2}(1 + (-1)^i)\gamma\right)}_{\mathbf{R}_\gamma(i)} l\mathbf{e}_1 \quad \forall i \in \mathscr{P} \qquad (31)$$

where $\gamma \in [0, \frac{\pi}{3}]$ and $l = \mathrm{dist}(O_B, O_{P_i}) > 0$. In this way the smallest angle between $\overline{O_B O_{P_i}}$ and $\overline{O_B O_{P_j}}$, $j = (i \bmod 6) + 1$ is alternatively $\frac{\pi}{3} - \gamma$ and $\frac{\pi}{3} + \gamma$, as shown in Fig. 1.

The orientation of the ith propeller is instead provided by

$$\mathbf{z}_{P_i} = \mathbf{R}_\gamma(i) \underbrace{\mathbf{R}_y(\beta)}_{\mathbf{R}_\beta} \underbrace{\mathbf{R}_x(\alpha_i)}_{\mathbf{R}_\alpha(i)} \mathbf{e}_3 = \mathbf{R}_{\alpha\beta\gamma}(i)\mathbf{e}_3 \qquad (32)$$

where $\mathbf{R}_x, \mathbf{R}_y$ are the canonical rotation matrices about the x-axis and y-axis, respectively, $\alpha_i = (-1)^{i-1}\alpha$ (with $i \in \mathscr{P}$), and $\alpha, \beta \in (-\frac{\pi}{2}, \frac{\pi}{2}]$. To geometrically understand the meaning of (32) one can note that the unit vector $\mathbf{z}_{P_i}$ is equal to the z-axis of the frame obtained after the following two consecutive rotations applied to $\mathscr{F}_B$: the first is a rotation of an angle α_i about the vector $\overrightarrow{O_B O_{P_i}}$, while the second is a rotation of an angle β about the y-axis of the intermediate frame obtained after the first rotation.

In terms of aerodynamic coefficients, each hexarotor of the family has the following alternating pattern:

$$c_{f_i} = c_f, \quad c_{\tau_i} = (-1)^{i-1} c_\tau \quad \forall i \in \mathscr{P} \qquad (33)$$

where c_f and c_τ are constants depending on the propellers.

In the following, we comment on the most relevant configurations that can be obtained by changing the three angles. First, when sweeping γ from 0 to $\frac{\pi}{3}$, we obtain a smooth transition between the two most popular propeller arrangements for hexarotors depicted in Fig. 2, i.e.,

1) $\gamma = 0$: the hexarotor has a *star-shape*, characterized by the fact that all the O_{P_i}s are located at the vertexes of a regular hexagon (see Fig. 2(a));

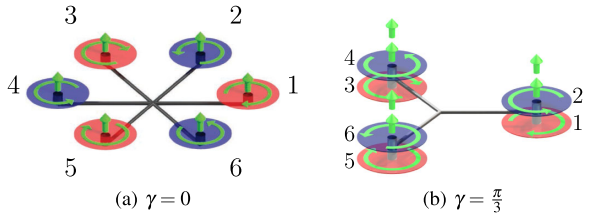

(a) $\gamma = 0$ (b) $\gamma = \frac{\pi}{3}$

Fig. 2. Two most popular $(0, 0, \gamma)$–hexarotor GTMs. (a) Standard star-shaped hexarotor ($\gamma = 0$). (b) Y-shaped hexarotor ($\gamma = \frac{\pi}{3}$).

2) $\gamma = \frac{\pi}{3}$: the hexarotor has a *Y-shape*, characterized by the fact that the O_{P_i}s are pairwise located at the vertexes of an equilateral triangle (see Fig. 2(b)). To make this configuration practically feasible there must be a suitable vertical distance between each pair of coincident propellers. However, this fact does not change the outcome of the following analysis, and therefore is neglected.

The angles α and β influence only the propeller orientations:

1) If both $\alpha = 0$ and $\beta = 0$, then the $\mathbf{z}_{P_i}$s are all pointing in the same direction as $\mathbf{z}_B$. This is the most common situation for standard hexarotors because it is the most efficient in terms of energy. However, it results in an under actuated dynamics due to the fact that $\mathrm{rank}(\mathbf{F}_1) = 1$.
2) If $\alpha \neq 0$ and $\beta = 0$, then the $\mathbf{z}_{P_i}$s are titled alternatively by an angle α and $-\alpha$ about the axes $\overrightarrow{O_B O_{P_1}}, \ldots, \overrightarrow{O_B O_{P_6}}$. This choice makes the GTM less energy efficient than the previous case. However, its advantage is that one can obtain $\mathrm{rank}(\mathbf{F}) = 6$, i.e., a D3 GTM.
3) If $\alpha = 0$ and $\beta \neq 0$, then the $\mathbf{z}_{P_i}$s are titled by an angle β about the axes passing through the O_{P_i}s and tangential to the circle passing through all the $O_{P_1}, \ldots, O_{P_6}$. This choice has the same full-actuation pros and energy efficiency cons of the previous case.
4) Finally, the case in which $\alpha \neq 0$ and $\beta \neq 0$ is a combination of the previous two.

TABLE II
ROLE OF THE ANGULAR PARAMETERS α, β, AND γ W.R.T. THE HEXAROTOR ACTUATION PROPERTIES

	role of α	role of β	role of γ
full-actuation	influential	influential	**un**influential
failure full robustness	**un**influential	influential	influential

The rest of the section is devoted to the analysis of the role of the angular parameters α, β, γ w.r.t. the rotor-failure robustness. Specifically, we study the conditions on these angles which make it possible to realize static hovering after a rotor loss. To this end, we denote by $\mathbf{G}_1(\alpha, \beta, \gamma), \mathbf{G}_2(\alpha, \beta, \gamma) \in \mathbb{R}^{3\times 6}$ the control force and moment input matrices of an (α, β, γ)-hexarotor (i.e., the $\mathbf{F}_1$ and $\mathbf{F}_2$ appearing in (8), respectively). In addition, we indicate as ${}^k\mathbf{G}_1(\alpha, \beta, \gamma)$ and ${}^k\mathbf{G}_2(\alpha, \beta, \gamma)$ the 3×5 matrices obtained from $\mathbf{G}_1(\alpha, \beta, \gamma)$ and $\mathbf{G}_2(\alpha, \beta, \gamma)$, respectively, by removing the kth column, i.e., assuming that the kth propeller fails, with $k \in \mathscr{P}$. Finally, for the sake of compactness, we summarize the propeller aerodynamic and geometric features using $r = (c_f/c_\tau)l$, while the symbols s and c stand for sine and cosine, respectively.

The formal results derived in the following are summed up in Table II that states the influence of the (α, β, γ) angles w.r.t. the full-actuation and the rotor-failure robustness.

B. On the Vulnerability of the (0,0,0)-Hexarotor GTMs

Before we proceed to analyze the role of the single angular parameters, we consider the case $\alpha = \beta = \gamma = 0$, which coincides with a standard star-shaped hexarotor. Although highly used, and often believed to be robust to failures, supposedly thanks to the presence of two additional rotors w.r.t. a quadrotor, these GTMs are actually *fully vulnerable*, as stated in the following proposition, which is a direct consequence of the two results shown independently in [23] and [24].

$$\mathbf{G}_2(0,0,0) = c_\tau \begin{bmatrix} 0 & \frac{\sqrt{3}}{2}r & \frac{\sqrt{3}}{2}r & 0 & -\frac{\sqrt{3}}{2}r & -\frac{\sqrt{3}}{2}r \\ -r & -\frac{1}{2}r & \frac{1}{2}r & r & \frac{1}{2}r & -\frac{1}{2}r \\ 1 & -1 & 1 & -1 & 1 & -1 \end{bmatrix} \tag{34}$$

$$\mathbf{G}_2(\alpha,0,0) = c_\tau \begin{bmatrix} 0 & \frac{\sqrt{3}}{2}(s\alpha + rc\alpha) & \frac{\sqrt{3}}{2}(s\alpha + rc\alpha) & 0 & -\frac{\sqrt{3}}{2}(s\alpha + rc\alpha) & -\frac{\sqrt{3}}{2}(s\alpha + rc\alpha) \\ -(s\alpha + rc\alpha) & -\frac{1}{2}(s\alpha + rc\alpha) & \frac{1}{2}(s\alpha + rc\alpha) & (s\alpha + rc\alpha) & \frac{1}{2}(s\alpha + rc\alpha) & -\frac{1}{2}(s\alpha + rc\alpha) \\ c\alpha - rs\alpha & -c\alpha + rs\alpha & c\alpha - rs\alpha & -c\alpha + rs\alpha & c\alpha - rs\alpha & -c\alpha + rs\alpha \end{bmatrix} \tag{35}$$

$$\mathbf{G}_2(0,\beta,0) = c_\tau \begin{bmatrix} s\beta & -\frac{1}{2}\left(s\beta - r\sqrt{3}c\beta\right) & -\frac{1}{2}\left(s\beta - r\sqrt{3}c\beta\right) & s\beta & -\frac{1}{2}\left(s\beta + r\sqrt{3}c\beta\right) & -\frac{1}{2}\left(s\beta + r\sqrt{3}c\beta\right) \\ -r\,c\beta & -\frac{1}{2}\left(\sqrt{3}s\beta + r\,c\beta\right) & \frac{1}{2}\left(\sqrt{3}s\beta + r\,c\beta\right) & r\,c\beta & -\frac{1}{2}\left(\sqrt{3}s\beta - r\,c\beta\right) & \frac{1}{2}\left(\sqrt{3}s\beta - r\,c\beta\right) \\ c\beta & -c\beta & c\beta & -c\beta & c\beta & -c\beta \end{bmatrix} \tag{36}$$

$$\mathbf{G}_2(0,0,\gamma) = c_\tau \begin{bmatrix} 0 & +r\,s\left(\frac{\pi}{3} - \gamma\right) & +r\,\frac{\sqrt{3}}{2} & +r\,s\left(\pi - \gamma\right) & -r\,\frac{\sqrt{3}}{2} & +r\,s\left(\frac{5\pi}{3} - \gamma\right) \\ -r & -r\,c\left(\frac{\pi}{3} - \gamma\right) & +r\,\frac{1}{2} & -r\,c\left(\pi - \gamma\right) & +r\,\frac{1}{2} & -r\,c\left(\frac{5\pi}{3} - \gamma\right) \\ 1 & -1 & 1 & -1 & 1 & -1 \end{bmatrix}. \tag{37}$$

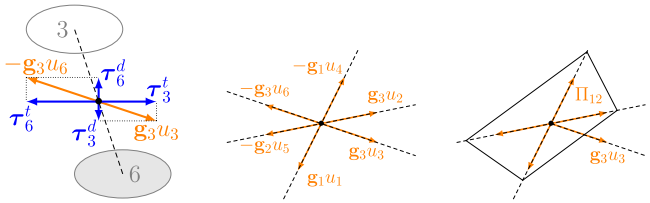

Fig. 3. Composition of the propeller moments for a $(\alpha, 0, 0)$-hexarotor GTM with any α. (a) Opposed rotors. (b) All healthy rotors. (c) Rotor-failure case.

Proposition 5 (Proposition 2 in [24]): The $(0, 0, 0)$–hexarotor GTM is fully vulnerable.

We provide next a new geometrical interpretation of this counterintuitive result which will help both to understand the result itself and to highlight the main drawback of the $(0, 0, 0)$–hexarotor design that should be overcome to attain the robustness against failure of such platforms.

Exploiting (31) and imposing $\alpha = \beta = \gamma = 0$, the control moment input matrix of the $(0, 0, 0)$–hexarotor GTM results as in (34)–(37) bottom of the previous page. Note that the columns $\{\mathbf{g}_i \in \mathbb{R}^3,\ i \in \mathscr{P}\}$ of $\mathbf{G}_2(0, 0, 0)$ are such that $\mathbf{g}_1 = -\mathbf{g}_4$, $\mathbf{g}_2 = -\mathbf{g}_5$, $\mathbf{g}_3 = -\mathbf{g}_6$. This means that the total moments generated by the two propellers of an opposed-propeller pair are always collinear regardless of the values assigned to their inputs u_i and u_j, where $(i, j) \in \{(1, 4), (2, 5), (3, 6)\}$ (see Fig. 3(a)), i.e., we have

$$\boldsymbol{\tau}_c = \mathbf{g}_1(u_1 - u_4) + \mathbf{g}_2(u_2 - u_5) + \mathbf{g}_3(u_3 - u_6). \tag{38}$$

According to (38), the total control moment applied to the platform can be expressed as the linear combination of the linearly independent vectors $\mathbf{g}_1, \mathbf{g}_2, \mathbf{g}_3$ that identify the directions of the moments of opposed-rotor pairs. Given that, even if $u_i, u_j \geq 0$, the sign of $(u_i - u_j)$ can be any, $\boldsymbol{\tau}_c$ can have any direction (and intensity) in $\mathbb{R}^3$ (see Fig. 3(b) for a graphical representation). However, if any propeller fails, e.g., propeller 6, then $u_6 = 0$ and the control moment degrades to

$$\boldsymbol{\tau}_c = \mathbf{g}_1(u_1 - u_4) + \mathbf{g}_2(u_2 - u_5) + \mathbf{g}_3u_3. \tag{39}$$

Given that u_3 in (39) must be nonnegative, $\boldsymbol{\tau}_c$ is limited in the half-space of $\mathbb{R}^3$ generated by $\mathbf{g}_3$ and by the delimiting plane Π_{12} parallel to $\mathbf{g}_1$ and $\mathbf{g}_2$, as graphically shown in Fig. 3(c). The condition (25) is therefore not satisfied, because any $\boldsymbol{\tau}$ belonging to the complementary half-space cannot be attained by any choice of $u_1 \dots u_5 \geq 0$.

We can summarize as follows:

1) the total moments generated by two propellers that are opposed are collinear; therefore,
2) the moments generated by two opposed-rotor pairs ($\mathbf{g}_1$, $\mathbf{g}_4$, $\mathbf{g}_2$, and $\mathbf{g}_5$ in Fig. 3(b)) lie all on a 2-dimensional (2-D) plane, even if they are generated by the (conical) combination of four independently controllable moments[4]; as a consequence,
3) five propellers alone can only generate half of the whole 3-D space.

[4]A conical combination of m vectors can contain in principle a subspace of dimension up to $m - 1$, i.e., up to 3 if $m = 4$.

If one finds a way to make the four moments at point 2) noncoplanar, but actually spanning (by conical combination) the whole space $\mathbb{R}^3$, then symmetry would be broken, singularity overcome, and robustness hopefully achieved. A way to obtain this is to design the hexarotor such that the moment of the opposed propeller pairs are not collinear as in the $(0, 0, 0)$-hexarotor case. We will show next by changing which ones of the angular parameters of the considered family of hexarotors one can actually achieve such goal.

C. Role of α

Despite the influential role of α in guaranteeing the full-actuation of the (α, β, γ)-hexarotor [7], [20], its effect in the robustness achievement is completely marginal, as summarized in the following statement.

Proposition 6: For any $\alpha \in (-\frac{\pi}{2}, \frac{\pi}{2}]$ the $(\alpha, 0, 0)$–hexarotor GTM is fully vulnerable.

Proof: The control moment input matrix is reported in (35). Both $\mathbf{G}_2(\alpha, 0, 0)$ and ${}^k\mathbf{G}_2(\alpha, 0, 0)$ (for any $k \in \mathscr{P}$) are full rank for every value of α in the domain of interest, except when $\tan(\alpha) = -r$ and $\tan(\alpha) = 1/r$. In fact, considering $\bar{\mathbf{G}}(\alpha, 0, 0) = \mathbf{G}_2(\alpha, 0, 0)\mathbf{G}_2^\top(\alpha, 0, 0) \in \mathbb{R}^{3\times3}$ and ${}^k\bar{\mathbf{G}}(\alpha, 0, 0) = {}^k\mathbf{G}_2(\alpha, 0, 0){}^k\mathbf{G}_2^\top(\alpha, 0, 0) \in \mathbb{R}^{3\times3}$, it holds that

$$\det(\bar{\mathbf{G}}(\alpha, 0, 0)) = 54c_\tau^2\,(s\alpha + rc\alpha)^4\,(c\alpha - rs\alpha)^2 \tag{40}$$

$$\det({}^k\bar{\mathbf{G}}(\alpha, 0, 0)) = 27c_\tau^2\,(s\alpha + rc\alpha)^4\,(c\alpha - rs\alpha)^2. \tag{41}$$

Trivially, (40) and (41) are null when $\tan(\alpha) = -r$ and $\tan(\alpha) = 1/r$, so in these two cases the requirement (11) is not satisfied and the hexarotor cannot hover statically.

For other cases, we focus the attention on the requirement (26), analyzing the $\ker({}^k\mathbf{G}_2(\alpha, 0, 0))$. Thanks to the particular structure of the matrix in (35), it can be seen that

$$\ker\left({}^k\mathbf{G}_2(\alpha, 0, 0)\right) = \operatorname{span}\left(\mathbf{h}_{k+1}^{\backslash k} + \mathbf{h}_{k-2}^{\backslash k},\ \mathbf{h}_{k+2}^{\backslash k} + \mathbf{h}_{k-1}^{\backslash k}\right) \tag{42}$$

where $\mathbf{h}_i^{\backslash k}$ is the vector of the canonical basis of $\mathbb{R}^5$ obtained in the following way:

1) first compute the vector of the canonical basis of $\mathbb{R}^6$, which has a one in the entry $i \bmod 6$ and zeros elsewhere,
2) then remove the kth entry from the previous vector (which is a zero entry by construction).

For example, for $k = 6$, we have $\mathbf{h}_{6+1}^{\backslash 6} = [1\ 0\ 0\ 0\ 0]^\top$ and $\mathbf{h}_{6-2}^{\backslash 6} = [0\ 0\ 0\ 1\ 0]^\top$ and therefore $\mathbf{h}_{6+1}^{\backslash 6} + \mathbf{h}_{6-2}^{\backslash 6} = [1\ 0\ 0\ 1\ 0]^\top$. Additionally we have $\mathbf{h}_{6+2}^{\backslash 6} + \mathbf{h}_{6-1}^{\backslash 6} = [0\ 1\ 0\ 0\ 1]^\top$. It is easy to check that the last two vectors are in $\ker({}^6\mathbf{G}_2(\alpha, 0, 0))$ regardless of the value of α. This implies that any $\mathbf{u} \in \mathbb{R}^5$ that satisfies ${}^6\mathbf{G}_2(\alpha, 0, 0)\mathbf{u} = \mathbf{0}$ has one entry structurally equal to 0 (corresponding to the propeller $k + 3 \bmod 6$), and therefore (26), cannot be satisfied. This finally means that the failed $(\alpha, 0, 0)$-hexarotor GTM cannot fly in static hovering, namely it is fully vulnerable according to Definition 6. ■

From a geometrical perspective, with reference to Fig. 3, tilting the propeller 3 of an angle α about $\overrightarrow{O_BO_{P_3}}$ and the propeller 6 of an angle $-\alpha$ about $\overrightarrow{O_BO_{P_6}}$ does tilt the two moments generated by the two opposite rotors in the same way and therefore keeps them collinear. The same holds for the pairs

$(1,4)$ and $(2,5)$. As a consequence, the discussion provided in Section V-B is still valid and the vulnerability of the $(\alpha,0,0)$-hexarotor is confirmed by the geometric intuition.

D. Role of β

The importance of β angle w.r.t. the capability of a star-shaped hexarotor to fly after a rotor failure has been discussed independently in [23] and [24]. Pushing further the understanding of this fact, in the following, we analytically and geometrically prove that a $(0,\beta,0)$-hexarotor GTM is also fully robust according to the stronger property defined in Definition 9.

Proposition 7: Assume that $\alpha=\gamma=0$, then for any $\beta\in(-\frac{\pi}{2},\frac{\pi}{2})$ such that $|\tan\beta|\neq\sqrt{3}r$ and $c^2\beta\neq\frac{1}{(1-r^2)}$, the resulting $(0,\beta,0)$-hexarotor GTM is fully robust.

Proof: When $\alpha=\gamma=0$, the control moment input matrix is parametrized by the angle β as in (36). Introducing $\bar{\mathbf{G}}(0,\beta,0)=\mathbf{G}_2(0,\beta,0)\mathbf{G}_2^\top(0,\beta,0)\in\mathbb{R}^{3\times3}$ and ${}^k\bar{\mathbf{G}}(0,\beta,0)={}^k\mathbf{G}_2(0,\beta,0){}^k\mathbf{G}_2^\top(0,\beta,0)\in\mathbb{R}^{3\times3}$, we first observe that

$$\det(\bar{\mathbf{G}}(0,\beta,0))=54c_\tau^2c^2\beta\left(1+(r^2-1)c^2\beta\right)^2 \tag{43}$$

$$\det({}^k\bar{\mathbf{G}}(0,\beta,0))=27c_\tau^2c^2\beta\left(1+(r^2-1)c^2\beta\right)^2. \tag{44}$$

Hence, the full-rankness (11) is guaranteed for any $\beta\in(-\frac{\pi}{2},\frac{\pi}{2})$ even in the case of any propeller failure, as long as $c^2\beta\neq\frac{1}{(1-r^2)}$.

Then, proceeding as in [23], we analyze the null space of the matrix ${}^k\mathbf{G}(0,\beta,0)$, assuming w.l.o.g. $k=6$. It can be seen that a generic vector $\mathbf{u}\in\ker({}^6\mathbf{G}(0,\beta,0))$ satisfies

$$u_1=\frac{\epsilon+1}{2\epsilon}u_3-\frac{\epsilon+1}{\epsilon-1},\qquad u_2=u_3-\frac{\epsilon+1}{\epsilon-1} \tag{45}$$

$$u_4=\frac{\epsilon+1}{2\epsilon}u_3+1,\qquad u_5=1 \tag{46}$$

where $\epsilon=-\frac{1}{\sqrt{3}r}\tan\beta\in\mathbb{R}$. Hence, supposing $0<|\epsilon|<1$, it can be proved that $\mathbf{u}\in\mathbb{R}^5$ defined in (45) and (46) is strictly positive if $0<u_3<|2\epsilon/(\epsilon+1)|$. As a consequence, the condition (26) is fulfilled.

Using the parametrization (45)–(46) for the vector $\mathbf{u}$, it can also be proved that the ${}^6\mathbf{G}_1(0,\beta,0)\mathbf{u}\neq\mathbf{0}$, where ${}^6\mathbf{G}_1(0,\beta,0)$ is obtained removing the sixth column of the force input matrix

$$\mathbf{G}_1(0,\beta,0)=\begin{bmatrix}s\beta & \frac{1}{2}s\beta & -\frac{1}{2}s\beta & -s\beta & -\frac{1}{2}s\beta & \frac{1}{2}s\beta\\ 0 & \frac{\sqrt{3}}{2}s\beta & \frac{\sqrt{3}}{2}s\beta & 0 & -\frac{\sqrt{3}}{2}s\beta & -\frac{\sqrt{3}}{2}s\beta\\ c\beta & c\beta & c\beta & c\beta & c\beta & c\beta\end{bmatrix}. \tag{47}$$

Having checked that the three conditions (11), (26), and (28) are met for any $\beta\in(-\frac{\pi}{2},\frac{\pi}{2})$ such that $|\tan\beta|\neq\sqrt{3}r$ and $c^2\beta\neq\frac{1}{(1-r^2)}$, then the statement of the proposition is proved. ■

This result can be also partially justified by geometric intuition. In fact, when all the propellers are equally inward/outward tilted of an angle $\beta\neq0$, the total moments of the opposed rotors are not collinear anymore. This is shown in Fig. 4(a) for propellers 3 and 6, where the vectors τ_3^d and τ_6^d are rotated in a way that breaks the symmetry while τ_3^t and τ_6^t have the same orientation as in Fig. 3(a) and are not shown. Thus, the moments of the opposed propellers, $\mathbf{g}_3u_3$ and $\mathbf{g}_6u_6$ in Fig. 4(a), are not collinear anymore and the same holds for the other two pairs of opposed propellers. The total moment is thus the conical combination of six different directions:

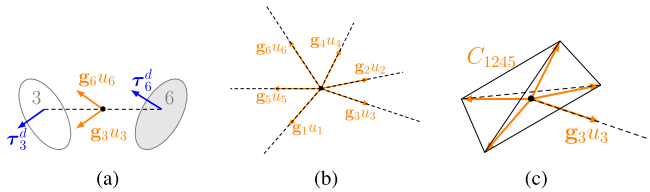

Fig. 4. Composition of the propeller moments for a $(0,\beta,0)$-hexarotor GTM with any $\beta\neq0$. (a) Opposed rotors. (b) All healthy rotors. (c) Rotor-failure case.

$$\boldsymbol{\tau}_c=\mathbf{g}_1u_1+\mathbf{g}_2u_2+\mathbf{g}_3u_3+\mathbf{g}_4u_4+\mathbf{g}_5u_5+\mathbf{g}_6u_6. \tag{48}$$

In this case, the failure of the sixth (or any other) propeller does not reduce the total control moment space since if we even only consider four of the five remaining vectors $\mathbf{g}_1,\mathbf{g}_2,\mathbf{g}_4,\mathbf{g}_5$ they are not anymore coplanar but actually their conical combination C_{1245} spans the whole $\mathbb{R}^3$, as depicted in Fig. 4(c). The same holds for the failure of any other propeller.

E. Role of γ

We conclude evaluating the role of γ. Note that the condition $\alpha=\beta=0$ and $\gamma\neq0$ entails that the propellers are parallel oriented but not equally spaced. This asymmetry of the platform results to be fundamental to overcome the vulnerability established in Section V-B.

Proposition 8: Assume that $\alpha=\beta=0$, then for any $\gamma\in(0,\frac{\pi}{3}]$, the resulting $(0,0,\gamma)$-hexarotor GTM is fully robust.

Proof: Imposing $\alpha=\beta=0$, the control moment input matrix is $\mathbf{G}_2(0,0,\gamma)$ in (37). This is full rank for any choice of $\gamma\in[0,\frac{\pi}{3}]$, and analogously is the derived ${}^k\mathbf{G}_2(0,0,\gamma)$ for any $k\in\mathscr{P}$. This fact can be verified by considering the determinant of the matrices $\bar{\mathbf{G}}_2(0,0,\gamma)=\mathbf{G}_2(0,0,\gamma)\mathbf{G}_2^\top(0,0,\gamma)\in\mathbb{R}^{3\times3}$ and ${}^k\bar{\mathbf{G}}_2(0,0,\gamma)={}^k\mathbf{G}_2(0,0,\gamma){}^k\mathbf{G}_2^\top(0,0,\gamma)\in\mathbb{R}^{3\times3}$. Specifically, it occurs that $\det(\bar{\mathbf{G}}_2(0,0,\gamma))=54c_\tau^2r^4$, hence the condition (11) is always fulfilled independently from γ. In the case of any rotor failure, the determinant of ${}^k\bar{\mathbf{G}}_2(0,0,\gamma)$ results instead to be a complex nonlinear function of γ, however it can be numerically checked that it is never null in the domain of interest. Hence, the first condition for the static hovering realizability is always satisfied in the case of rotor-failure.

To explore which conditions on γ possibly ensure that ${}^k\mathbf{G}_2(0,0,\gamma)$ fulfills requirement (26), we assume again that the sixth rotor fails. The solution of ${}^6\mathbf{G}_2(0,0,\gamma)\mathbf{u}=\mathbf{0}$ is

$$u_1=u_4+\frac{(-\sqrt{3}s\gamma-c\gamma+1)}{(2c\gamma+1)} \tag{49}$$

$$u_2=-\frac{\left(\sqrt{3}s\gamma-c\gamma+1\right)}{(2c\gamma+1)}u_4+\frac{3}{(2c\gamma+1)} \tag{50}$$

$$u_3=-\frac{\left(\sqrt{3}s\gamma-c\gamma+1\right)}{(2c\gamma+1)}u_4+\frac{\left(\sqrt{3}s\gamma-c\gamma+1\right)}{(2c\gamma+1)} \tag{51}$$

$$u_5=1. \tag{52}$$

It can be verified that, as expected, the positivity of $\mathbf{u}$ cannot be ensured for $\gamma=0$. In fact, replacing $\gamma=0$ in (51), we obtain

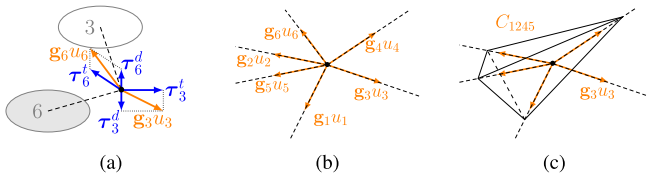

Fig. 5. Composition of the propeller moments for a $(0, 0, \gamma)$-hexarotor GTM with $\gamma = \frac{\pi}{3}$. (a) Opposed rotors. (b) All healthy rotors. (c) Rotor-failure case.

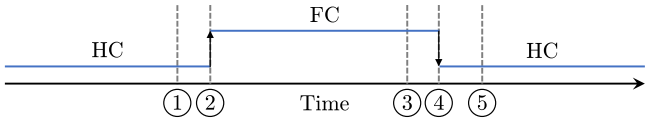

Fig. 6. Time line of controller switching. (1) HC is running, failure is manually triggered—ith propeller stops. (2) Failure gets detected, opposing propeller is stopped and controller switched to FC. (3) Manual trigger to restart the two stopped motors. (4) Two rotors reach 16 Hz, the controller is switched back to HC. (5) Reference trajectory reaches the initial position and orientation of the Tilt-Hex.

$u_3 = 0$, a structurally zero entry, as in the proof of Proposition 6. On the other side, observing that $0 \leq s\gamma \leq \frac{\sqrt{3}}{2}$ and $\frac{1}{2} \leq c\gamma \leq 1$ in the domain of interest, the condition $0 < \gamma < \pi/3$ implies the existence of a strictly positive vector $\mathbf{u} \in \ker({}^6\mathbf{G}_2(0, 0, \gamma))$, namely the fulfillment of (26).

Exploiting (49)–(52), it is possible to show that also (28) is satisfied when $\gamma > 0$. To do so, it is necessary to evaluate ${}^6\mathbf{G}_1(0, 0, \gamma)\mathbf{u}$ by introducing the control force input matrix

$$\mathbf{G}_1(0, 0, \gamma) = c_f \, [\mathbf{e}_3 \ \mathbf{e}_3 \ \mathbf{e}_3 \ \mathbf{e}_3 \ \mathbf{e}_3 \ \mathbf{e}_3] \tag{53}$$

Trivially, it results that ${}^6\mathbf{G}_1(0, 0, \gamma)\mathbf{u} \neq \mathbf{0}$. As a consequence, both the Y-shape hexarotor ($\gamma = \frac{\pi}{3}$) and all the less common configurations where $0 < \gamma < \frac{\pi}{3}$ are fully robust. ■

Fig. 5(a) shows the moments composition for a pair of opposed rotors in a Y-shaped hexarotor. It is straightforward to see that whenever $\gamma > 0$ the moment directions of the opposed propellers are not collinear anymore. This generates the same beneficial consequences described in Section V-D, as shown in Fig. 5(b) and (c). For example, the conical combination C_{1245} spans the whole $\mathbb{R}^3$ also in this case.

VI. Experiments With a Star-Shaped Hexarotor

In this section, we present and discuss real-world experiments that have been conducted on a star-shaped hexarotor platform available at LAAS-CNRS, the Tilt-Hex.

A. Experimental Setup

The Tilt-Hex aerial robot is a fully actuated (and therefore un-coupled/fully decoupled) multirotor, developed at LAAS-CNRS. It is a $(\frac{7\pi}{36}, \frac{5\pi}{36}, 0)$–hexarotor GTM, namely is an instantiation of a star-shaped hexarotor whose propellers are tilted with $\alpha = 35°$ and $\beta = 25°$. These angles represent a good choice to achieve a balance between full actuation and inefficient losses as a result of internal forces. In addition, the choice of no-zero α entails some practical advantages also in the case of a motor-fail that will be clear in the following.

All the mechanical parts of the Tilt-Hex are off-the-shelf available or 3-D printable. The diameter of the platform, including the propeller blades, is 1.05 m and the total mass, with a 2200 mAh Li-Po battery, results as $m = 1.8$ kg.

The MK3638 brushless motors by MikroKopter are used, together with 12 in propeller blades. A single propeller–motor combination can provide a maximum thrust of 12 N. The ESC (electronic speed controller), a Bl-Ctrl-2.0, is as well purchased from MikroKopter. The control software running on the ESC, developed at LAAS, controls the rotational propeller speed in closed loop and additionally allows to read the current spinning rate [27]. An on-board inertial measurement unit (IMU) provides measurements of three gyroscopes and a 3-D accelerometer at 500 Hz. An OptiTrack motion capture system provides position and orientation data at 100 Hz. These data are fused via a UKF state estimator to obtain the full vehicle state at 500 Hz.

The controller is implemented in MATLAB-Simulink and runs at 500 Hz on a stationary workstation. As its computational effort is very low (considerably below 1 ms per control loop), it could be ported easily to an on-board system. Based on our experience with a similar porting, we expect the performances of the onboard implementation to be better than the MATLAB-Simulink implementation, thanks to the possibility of reaching a faster control frequency (greater than 1 kHz) and latency below 1 ms. Therefore, the experiments shown here represent a worst case scenario from this point of view.

During the execution of all experiments, two controllers have been utilized (see Fig. 6). While the Tilt-Hex is healthy (all rotors working) or before a failure detection of an ESC, the controller presented in [20] and [28] is used—referred to as the *healthy controller* (HC). As soon as a failure is detected, the controller is switched to the controller described in [24]—referred to as *failed controller* (FC).[5] In some of the following experiments, the failure of the ESC has been triggered externally. The fail trigger lets an ESC to immediately stop its propeller from spinning and to rise a failure flag. The status of the failure flags of all ESCs is checked every 10 ms. When a failure is detected, the opposed propeller is stopped and the controller is switched to FC. To change back the status from failed to healthy, the two stopped motors need to be restarted. As the time duration is not always identical, the FC is used until a spinning rate of 16 Hz (minimum closed-loop spinning rate of the ESC) is reached on both previously stopped motors. Then, the controller is switched to HC and a trajectory is computed to drive back the platform from its current position and orientation to the initial reference position and orientation smoothly. Finally, the Tilt-Hex reaches its initial position and orientation.

We used external failure triggers for conducting several experiments in a row and in a repeatable way. In addition, we also performed an experiment where a propeller was mechanically stopped by an impact with an external object during flight. Fig. 7 reports some significant frames of the experiment with the mechanical stop. This shows the robustness of the proposed approach and the possibility of using it within a pipeline of failure

[5]We reused in this section the acronym "FC" for failed controller since there is not risk to confuse it with "fully coupled."

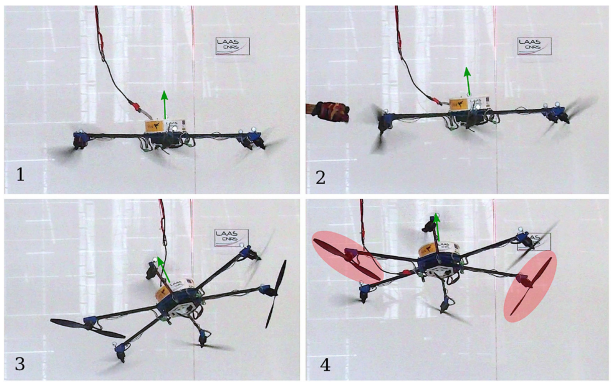

Fig. 7. Recovering of the Tilt-Hex from the manual hitting of one of its propeller. The numbers indicate the different phases of the experiment. (1) Static hover in healthy conditions. (2) Manual stop of a propeller. (3) Transient phase. (4) Static hovering in failed conditions (nonspinning propellers are marked in red).

detection, isolation, and reaction. The reader is referred to the videos attached to this paper to fully enjoy all these experiments.

B. Experimental Validations

1) Basic Principles: In the first experiment (Experiment 1), we present the basic principles and behavior of the controller and its recovering capabilities. We report the results of three consecutive failures of the first three propellers, resulting in the stopping of all propeller pairs (1–4, 2–5, 3–6) of the Tilt-Hex. To perform the experiment, we have as well recovered from the failed situation and restarted the failed and the actively stopped motor (compare Fig. 6). As the Tilt-Hex is a fully actuated aerial vehicle, a smooth transient trajectory is followed to recover the initial pose after the motor failure phase.

The results of Experiment 1 are presented in Fig. 8. The background colors of the plots indicate the used controller. In green shaded areas HC is used, in red shaded areas FC is used while in white shaded areas FC is used as well but the two stopped motors are restarted already. The first two plots of Fig. 8 present the reference position $\mathbf{p}_r$, the actual position $\mathbf{p}$, and the position error $\mathbf{e}_p = \mathbf{p} - \mathbf{p}_r$ irrespective of the used controller. Note that initially, while HC is used, the reference position is tracked perfectly. At $t_1 = 7.58$ s the failure of motor 1 is triggered (corresponding to event 1 in Fig. 6) and at $t_2 = 7.6$ s the controller is switched to FC and the opposed motor 4 is stopped (corresponding to event 2 in Fig. 6). Immediately the position error increases, reaching a peak position error norm of $\|\mathbf{e}_p\| = 0.37$ m. In the moment of controller switching, a discontinuity of the reference orientation $\mathbf{R}_r$ occurs. This is evident comparing the third and fourth plot of Fig. 8: the third plot reports the current and reference orientation expressed in terms of roll-pitch-yaw angles, while the fourth plot depicts the orientation error, defined as $\mathbf{e}_R = \frac{1}{2}(\mathbf{R}_r^\top \mathbf{R} - \mathbf{R}^\top \mathbf{R}_r)^\vee$, where the operator $[\cdot]^\vee$ describes the map from the $\mathfrak{so}(3)$ to $\mathbb{R}^3$. The discontinuity is explained by the different steady hovering orientations of the failed system, which is due to the presence of no-zero tilt angle α. Indeed, setting $\alpha \neq 0$ implies that, when a motor fails, the PC resulting platform has a decoupled direction which is not parallel to $\mathbf{z}_B$.

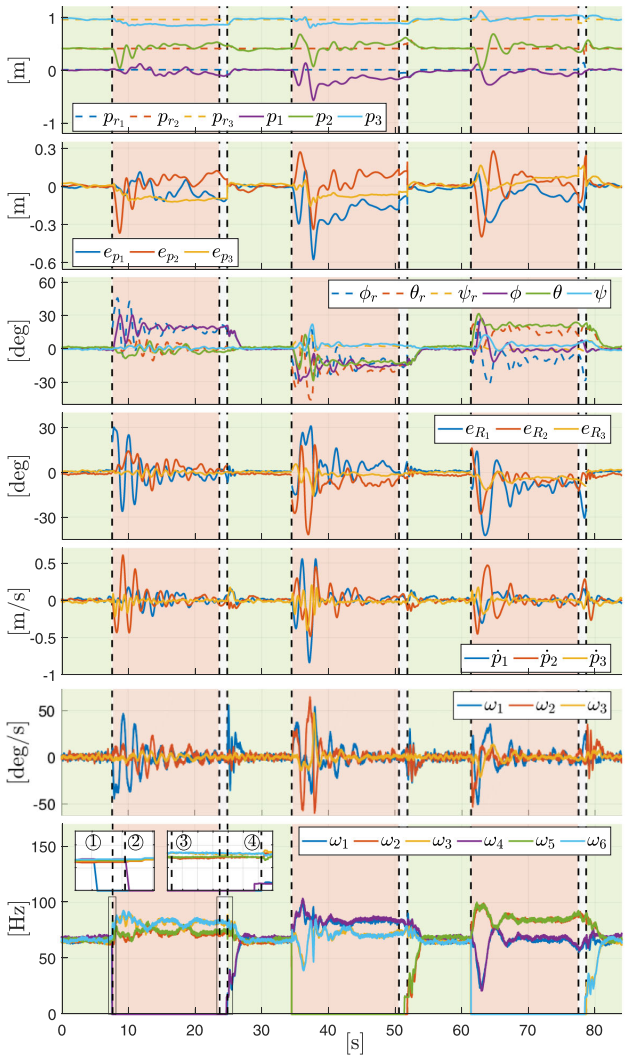

Fig. 8. Experiment 1—three consecutive failure and recovery of motor 1 till motor 3. Green shaded background—Tilt-Hex healthy; Red shaded background—Tilt-Hex rotor failed; White shaded background—FC but stopped propellers are restarted already.

However, it implies also a smaller condition number for the matrix ${}^k\mathbf{G}_2(\frac{7\pi}{36}, \frac{5\pi}{36}, 0)$ that has to be inverted in the computation of the input required to achieve the reference control moment (see [24] for further details).

After the controller switching, the system stabilizes within a few seconds (observe $\dot{\mathbf{p}}$ and $\boldsymbol{\omega}$ in Fig. 8). The final orientation error is negligible, while a small steady-state position error is still visible, which can be easily explained by the unavoidable uncertainty in the force and torque coupling matrices in (8). This error can be further decreased using integral terms or adaptive control, however the main goal here was to show that static hovering (i.e., with zero velocities) is achieved, rather than showing extremely accurate position control. At $t_3 = 23.7$ s the two stopped motors are asked to start again and at $t_3 = 24.8$ s both rotors are spinning with the minimum spinning rate $\omega_{1,4} = 16$ Hz of the ESC. The controller is switched to HC and the initial position and orientation is reached fast without any visual steady-state error. The same procedure is repeated for motor $i = 2$ and $i = 3$. In

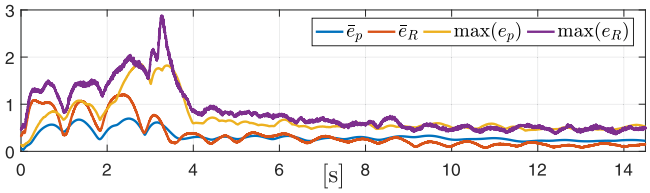

Fig. 9. Experiment 2-1—Mean of state error function for 23 trials in position (blue) and orientation (red) and maximum state error values over all trials (yellow and purple).

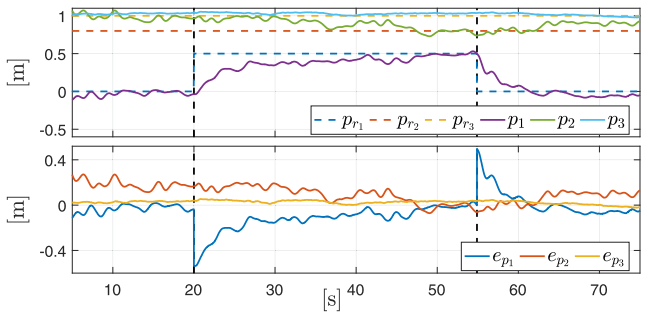

Fig. 10. Experiment 2-2—Step response of the system with failure. At $t = 20$ s a step of 0.5 m along p_{r_1} is commanded. At $t = 55$ s a step of -0.5 m along p_{r_1} is commanded. The time of the step signal is indicated by the black dashed line in all plots.

the three failed phases different motor pairs are stopped: it is interesting to notice the different hovering orientations during the different failures.

2) Robustness: We now test the robustness of the controller by three experiments. In Experiment 2-1, we present accumulated results of $n = 23$ repeated failures of motor 3, and in Experiment 2-2, we show the response of the system in the case of a step in the reference position under failed conditions. Finally, in Experiment 2-3, we present the response of the system to a continuously changing reference (similar to a ramp response).

In Experiment 2-1, the last phase of Experiment 1 (from 60 to 80 s) has been repeated for 23 trials: the Tilt-Hex has recovered from the failure in all the cases. To get a better understanding of the vehicle performance, we define a new position and orientation error function representing the error of its state

$$e_p = \|\mathbf{e}_p\| + k\|\mathbf{e}_v\|, \qquad e_R = \|\mathbf{e}_R\| + k\|\mathbf{e}_w\|$$

with $k = 1$ s, $\mathbf{e}_v = \dot{\mathbf{p}}$, and $\mathbf{e}_\omega = \boldsymbol{\omega}$. In Fig. 9, we report the mean error value $\bar{e}_p$ and $\bar{e}_R$ of all trials, and their maximum value at each time instant. The failure is triggered at $t = 0$ s, and it is evident that the position and orientation state error increases directly after the failure but then decreases after ≈ 2.5 s and stabilizes at small values after ≈ 4 s. Similarly, the maximum of the state error increases in the beginning, reaches its maximum after ≈ 2.5 s but then decreases rapidly.

In Experiment 2-2, (see Fig. 10) a step in the reference position $\mathbf{p}_r$ of 0.5 m is commanded at $t = 20$ s under failed condition (FC). At $t = 55$ s an opposing step of -0.5 m is commanded. The Tilt-Hex tracks both steps within a few seconds and the platform position and orientation remains perfectly stable.

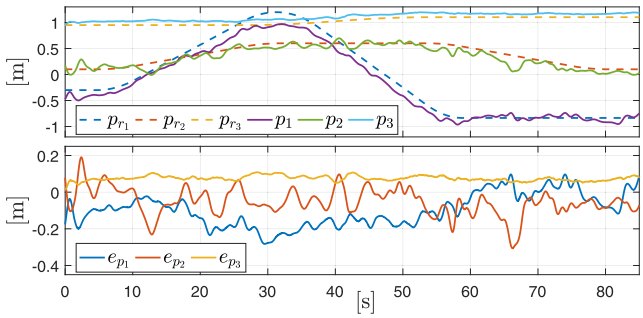

Fig. 11. Experiment 2-3—Trajectory following of the system with failure.

TABLE III
STANDARD DEVIATIONS OF THE SIMULATED NOISE

p	$\dot{\mathbf{p}}$	**R**	$\boldsymbol{\omega}$	**u**
6.4e-04	1.4e-03	1.2e-03	2.7e-03	0-0.32

In Experiment 2-3, the reference position trajectory is changed about all axes with a total trajectory length of 2.4 m (see Fig. 11, first plot) while the reference orientation is horizontal ($\mathbf{R}_r = \mathbf{I}_3$). The position error remains limited with a maximum norm position error of $\max|\mathbf{e}_p| = 0.3$ m at 59 s. Note that the failed Tilt-Hex is actually more difficult to control than an ordinary underactuated system (e.g., a standard quadrotor). In the case of a collinear multirotor system, the generated thrust force is always perpendicular to the rotor plane regardless of the rotational speed of each rotor. In the case of the failed Tilt-Hex, this property is not given anymore, making the tracking of time varying trajectories much more difficult.

VII. SIMULATIONS WITH A Y-SHAPED HEXAROTOR

Given that a Y-shaped hexarotor (namely a $(0, 0, \frac{\pi}{3})$-hexarotor GTM) is not available for testing in our lab, we tested the theoretical results regarding this kind of hexarotor in a realistic simulation for the case of a single propeller failure. The simulation exploits the dynamic model (8) extended by several real-world effects to increase the fidelity.

1) Position and orientation feedback and their derivatives are impinged on time delay t_f =12 ms and sensor noise according to Table III. The actual position and orientation are fed back with a lower sampling frequency of only 100 Hz while the controller runs at 500 Hz. These properties are reflecting a typical motion capture system and an IMU seen in the experiments of Section VI.
2) The ESC driving the motors is simply modeled by quantizing the desired input $\mathbf{u}$ resembling a 10 b discretization in the feasible motor speed resulting in a step size of ≈ 0.12 Hz. Additionally, the motor–propeller combination is modeled as a first-order transfer function $(G(s) = \frac{1}{1+0.005\,\mathrm{s}})$. The resulting signal is loaded again with a rotational velocity dependent noise level (see Table III). This combination mirrors with high realism the dynamic behavior of a common ESC motor–propeller

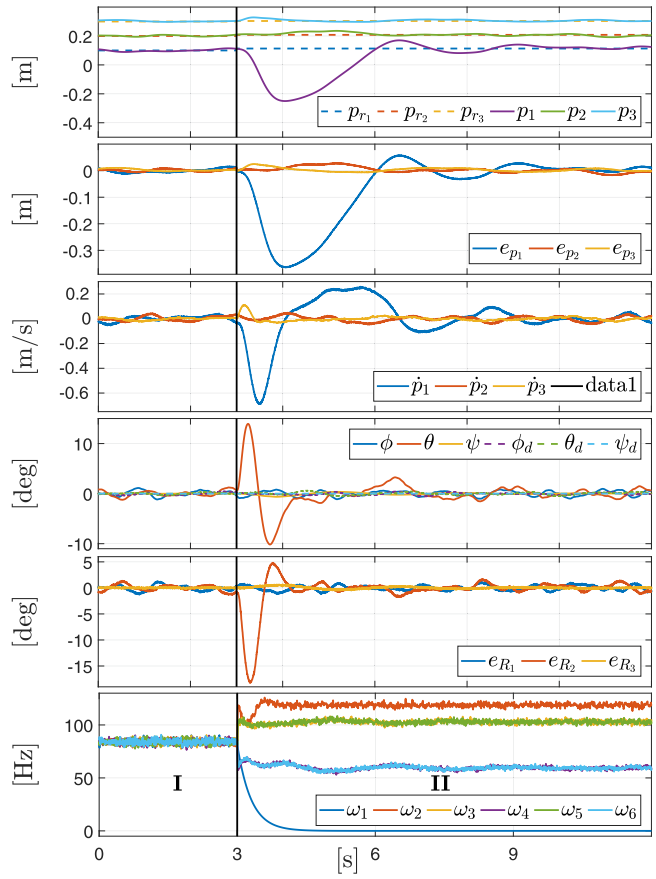

Fig. 12. Realistic simulation of the control of a Y-shaped hexarotor GTM in the case of a motor failure. The moment of motor failure is indicated by the black vertical bar.

combination [27] (i.e., BL-Ctrl-2.0, by MikroKopter, Robbe ROXXY 2827-35 and a 10 in rotor blade).

3) The controller assumes a direct stop of the failed propeller, whereas in the model an exponential decay of the failed rotor' generated force is simulated ($t_{\frac{1}{2}} = 0.1$ s). This adds an unknown force and torque disturbance.

In the simulated scenario the vehicle shall hover at a predefined spot $\mathbf{p}_r$ and $\mathbf{R}_r$ (*phase I*). At time $t = 3$ s, we model the failure of a single rotor and use the controller described in [24] to recover from this situation (*phase II*). The actual position in the moment of failure is used as new reference position.

The results of the Y-shaped hexarotor simulation are reported in Fig. 12. The position and orientation errors (plot 1 and plot 4) in phase I (before the failure occurs) are negligible—the hexarotor hovers perfectly at its desired spot. Accordingly, the translational velocity (plot 2) is very small (considering the realistic factors introduced in the simulation) with $\|\dot{\mathbf{p}}\| < 0.07$ m/s. At time $t = 3$ s, the failure of propeller 1 is simulated. The actual spinning rates $\omega_1, \ldots, \omega_6$ are reported in the last plot of Fig. 12. In the moment of rotor 1 failure ω_1 starts to decrease exponentially and the system is clearly perturbed. Immediately the translational velocity and the position error are increasing, reaching a peak position error of $\|\mathbf{e}_p\| = 0.46$ m 1.1 s after the failure. Subsequent, the position and orientation errors decrease fast and the hexarotor GTM tracks again well the reference position. It is interesting to see how propeller 2, 3, and 5 are compensating the loss of generated thrust while propellers 4 and 6 are commanded to decrease their thrust.

In [24], we already presented simulated results for a tilted star-shaped hexarotor. Compared to this case, on a Y-shaped hexarotor, it is not advisable to switch off the propeller opposed to the failed one as in the star-shaped case.

VIII. Conclusion and Future Work

In this paper, we studied two fundamental actuation properties for the multirotor UAVs. First, we considered the interplay between the control force and the control moment and we distinguished between FC, PC, and UC platforms according to both the dimension of the freely assignable force subspace $\mathfrak{F}_B$ and its relation with the total force subspace $\mathfrak{F}$. Then, we introduced the concept of static hovering realizability that rests upon the possibility to reject any disturbance torque while counterbalancing the gravity. The robustness properties of a family of hexarotor parametrized by three angles have been finally explored in terms of capability to statically hover after a rotor loss. We found out that the full robustness is guaranteed by (inward/outward) tilting each propeller on its $\overrightarrow{O_B O_{P_i}}$-axis or by moving towards the Y-shaped hexarotor and thus breaking the symmetry of the propeller positions in the star-shaped hexarotor.

It should be straightforward for other research groups to apply the theory developed in this paper to assess the robustness other classes of vehicles with $n = 6$ or more and whose angular parameters can even change during flight.

An interesting challenge would be also to design a n-rotor platform that is (fully) robust to the loss of $(n-4)$ propellers, e.g., a fully 2-losses robust hexarotor, or a fully 3-losses robust eptarotor, or a fully 4-losses robust octorotor. Indeed, if such platform exists or not is still an open question.

Acknowledgemnt

The authors would like to thank A. Mallet (LAAS–CNRS) for his contribution in the software architecture of the experiments.

References

[1] V. Duggal, M. Sukhwani, K. Bipin, G. S. Reddy, and K. M. Krishna, "Plantation monitoring and yield estimation using autonomous quadcopter for precision agriculture," in *Proc. 2016 IEEE Int. Conf. Robot. Autom.*, Stockholm, Sweden, May 2016, pp. 5121–5127.

[2] J. Park and Y. Kim, "Horizontal-vertical guidance of quadrotor for obstacle shape mapping," *IEEE Trans. Aerosp. Electron. Syst.*, vol. 52, no. 6, pp. 3024–3035, Dec. 2016.

[3] D. Mellinger, M. Shomin, N. Michael, and V. Kumar, "Cooperative grasping and transport using multiple quadrotors," in *Proc. 10th Int. Symp. Distrib. Auton. Robot. Syst.*, Lausanne, Switzerland, Nov. 2010, pp. 545–558.

[4] R. Spica, A. Franchi, G. Oriolo, H. H. Bülthoff, and P. Robuffo Giordano, "Aerial grasping of a moving target with a quadrotor UAV," in *Proc. 2012 IEEE/RSJ Int. Conf. Intell. Robots Syst.*, Vilamoura, Portugal, Oct. 2012, pp. 4985–4992.

[5] B. Yüksel, C. Secchi, H. H. Bülthoff, and A. Franchi, "Reshaping the physical properties of a quadrotor through IDA-PBC and its application to aerial physical interaction," in *Proc. 2014 IEEE Int. Conf. Robot. Autom.*, Hong Kong, May 2014, pp. 6258–6265.

[6] B. Yüksel, C. Secchi, H. H. Bülthoff, and A. Franchi, "A nonlinear force observer for quadrotors and application to physical interactive tasks," in *Proc. 2014 IEEE/ASME Int. Conf. Adv. Intell. Mechatronics*, Besançon, France, Jul. 2014, pp. 433–440.

[7] S. Rajappa, M. Ryll, H. H. Bülthoff, and A. Franchi, "Modeling, control and design optimization for a fully-actuated hexarotor aerial vehicle with tilted propellers," in *Proc. 2015 IEEE Int. Conf. Robot. Autom.*, Seattle, WA, USA, May 2015, pp. 4006–4013.
[8] D. Brescianini and R. D'Andrea, "Design, modeling and control of an omni-directional aerial vehicle," in *Proc. 2016 IEEE Int. Conf. Robot. Autom.*, Stockholm, Sweden, May 2016, pp. 3261–3266.
[9] S. Park, J. J. Her, J. Kim, and D. Lee, "Design, modeling and control of omni-directional aerial robot," in *Proc. 2016 IEEE/RSJ Int. Conf. Intell. Robots Syst.*, Daejeon, South Korea, 2016, pp. 1570–1575.
[10] V. G. Adîr, A. M. Stoica, and J. F. Whidborne, "Modelling and control of a star-shaped octorotor," *Appl. Mech. Mater.*, vol. 325, pp. 994–998, 2013.
[11] S. J. Haddadi and P. Zarafshan, "Design and fabrication of an autonomous octorotor flying robot," in *Proc. 3rd RSI Int. Conf. Robot. Mechatronics*, Tehran, Iran, Oct. 2015, pp. 702–707.
[12] M. Tognon and A. Franchi, "Omnidirectional aerial vehicles with unidirectional thrusters: Theory, optimal design, and control," *IEEE Robot. Autom. Lett.*, vol. 3, no. 3, pp. 2277–2282, Jul. 2018.
[13] N. Staub, M. Mohammadi, D. Bicego, D. Prattichizzo, and A. Franchi, "Towards robotic MAGMaS: Multiple aerial-ground manipulator systems," in *Proc. 2017 IEEE Int. Conf. Robot. Autom.*, Singapore, May 2017, pp. 1307–1312.
[14] P. Katsigiannis, L. Misopolinos, V. Liakopoulos, T. K. Alexandridis, and G. Zalidis, "An autonomous multi-sensor UAV system for reduced-input precision agriculture applications," in *Proc. 24th Mediterranean Conf. Control Autom.*, Athens, Greece, Jun. 2016, pp. 60–64.
[15] M. Makarov *et al.*, "Octorotor UAVs for radar applications: Modeling and analysis for control design," in *Proc. Workshop Res., Edu. Develop. Unmanned Aerial Syst.*, Linköping, Sweden, Nov. 2015, pp. 288–297.
[16] M. Ryll *et al.*, "6D physical interaction with a fully actuated aerial robot," in *Proc. 2017 IEEE Int. Conf. Robot. Autom.*, Singapore, May 2017, pp. 5190–5195.
[17] M. Kamel, K. Alexis, M. Achtelik, and R. Siegwart, "Fast nonlinear model predictive control for multicopter attitude tracking on SO(3)," in *Proc. 2015 IEEE Conf. Control Appl.*, Sydney, NSW, Australia, Sep. 2015, pp. 1160–1166.
[18] M. Ryll, H. H. Bülthoff, and P. Robuffo Giordano, "A novel overactuated quadrotor unmanned aerial vehicle: Modeling, control, and experimental validation," *IEEE Trans. Control Syst. Technol.*, vol. 23, no. 2, pp. 540–556, Mar. 2015.
[19] A. Nemati and M. Kumar, "Modeling and control of a single axis tilting quadcopter," in *Proc. 2014 Amer. Control Conf.*, Portland, OR, USA, Jun. 2014, pp. 3077–3082.
[20] M. Ryll, D. Bicego, and A. Franchi, "Modeling and control of FAST-Hex: A fully-actuated by synchronized-tilting hexarotor," in *Proc. 2016 IEEE/RSJ Int. Conf. Intell. Robots Syst.*, Daejeon, South Korea, Oct. 2016, pp. 1689–1694.
[21] G. X. Du, Q. Quan, B. Yang, and K. Cai, "Controllability analysis for multirotor helicopter rotor degradation and failure," *AIAA J. Guid., Control, Dyn.*, vol. 38, no. 5, pp. 978–985, 2015.
[22] H. Mehmood, T. Nakamura, and E. N. Johnson, "A maneuverability analysis of a novel hexarotor UAV concept," in *Proc. 2016 Int. Conf. Unmanned Aircraft Syst.*, Arlington, VA, USA, Jun. 2016, pp. 437–446.
[23] J. I. Giribet, R. S. Sanchez-Pena, and A. S. Ghersin, "Analysis and design of a tilted rotor hexacopter for fault tolerance," *IEEE Trans. Aerosp. Electron. Syst.*, vol. 52, no. 4, pp. 1555–1567, Aug. 2016.
[24] G. Michieletto, M. Ryll, and A. Franchi, "Control of statically hoverable multi-rotor aerial vehicles and application to rotor-failure robustness for hexarotors," in *Proc. 2017 IEEE Int. Conf. Robot. Autom.*, Singapore, May 2017, pp. 2747–2752.
[25] D. Falanga, E. Mueggler, M. Faessler, and D. Scaramuzza, "Aggressive quadrotor flight through narrow gaps with onboard sensing and computing using active vision," in *Proc. 2017 IEEE Int. Conf. Robot. Autom.*, Singapore, Jun. 2017, pp. 5774–5781.
[26] D. Scaramuzza *et al.*, "Vision-controlled micro flying robots: From system design to autonomous navigation and mapping in GPS-denied environments," *IEEE Robot. Autom. Mag.*, vol. 21, no. 3, pp. 26–40, Sep. 2014.
[27] A. Franchi and A. Mallet, "Adaptive closed-loop speed control of BLDC motors with applications to multi-rotor aerial vehicles," in *Proc. 2017 IEEE Int. Conf. Robot. Autom.*, Singapore, May 2017, pp. 5203–5208.
[28] A. Franchi, R. Carli, D. Bicego, and M. Ryll, "Full-pose tracking control for aerial robotic systems with laterally-bounded input force," *IEEE Trans. Robot.*, vol. 34, no. 2, pp. 534–541, 2018.

Giulia Michieletto received the Master's degree in automation engineering and the Ph.D. degree in information engineering from University of Padova, Italy, in 2014 and 2017, respectively.

From March 2016 to February 2017, she was a Visiting Researcher with LAAS-CNRS, Toulouse, France. Since 2018, she has been a Postdoctoral Fellow with University of Padova. Her current research interests include analysis, estimation, and control of multiagent systems acting in smart environments.

Markus Ryll (M'15) received the Diploma in mechatronics from Hochschule Karlsruhe in 2008 and the Master's degree in medical engineering from Hochschule Ulm in 2010. He received the Ph.D. degree in robotics from Max Planck Institute for Biological Cybernetics, Tübingen, Germany, in cooperation with University of Stuttgart, Stuttgart, Germany, in 2015.

From 2014 to 2017, he was a Research Scientist with the RIS team, LAAS-CNRS, Toulouse, France. Since 2018, he has been a Senior Research Scientist with the Robust Robotics Group, Massachusetts Institute of Technology, Cambridge, MA, USA. His main research interests include design modeling and control of novel robotic systems, mainly focused on aerial platforms.

Antonio Franchi (S'07–M'11–SM'16) received the Ph.D. degree in system engineering from Sapienza University of Rome, Rome, Italy, in 2010 and the Habilitation to Direct Research (HDR) in Sciences from National Polytechnic Institute of Toulouse, Toulouse, France, in 2016.

In 2009, he was a Visiting Scholar with University of California at Santa Barbara, Santa Barbara, CA, USA. From 2010 to 2014, he was first a Research Scientist and then a Senior Research Scientist and the Project Leader of the Autonomous Robotics and Human Machine Systems Group, Max Planck Institute for Biological Cybernetics in Tübingen, Germany. Since 2014, he has been a Tenured CNRS Researcher with the RIS team, LAAS-CNRS, Toulouse, France. He published more than 100 papers in peer-reviewed international journals and conferences. His main research interests include autonomous systems, with a special regard to robot control and estimation, particularly for multiple-robot systems and aerial robotics.

Dr. Franchi received the IEEE RAS ICYA Best Paper Award in 2010. He is an Associate Editor for IEEE TRANSACTIONS ON ROBOTICS. He is the co-founder of the IEEE RAS Technical Committee on Multiple Robot Systems and of the International Symposium on Multi-Robot and Multi-Agent Systems.